KATHOLIEKE
UNIVERSITEIT
LEUVEN

Nanostructured Superconductors:

How to enhance Vortex Pinning and Critical Fields?

V. V. Moshchalkov

Talk presented at:
Boulder 2000 Summer School for Condensed Matter and Materials Physics
Introduction to Superconductivity: Fundamentals and Applications

Laboratorium voor Vaste-Stoffysica en Magnetisme

Nanostructured Superconductors: How to enhance Vortex Pinning and Critical Fields? [1]

V. V. Moshchalkov, V. Bruyndoncx, L. Van Look,
M. J. Van Bael, and Y. Bruynseraede

Laboratorium voor Vaste-Stoffysica en Magnetisme,
Katholieke Universiteit Leuven,
Celestijnenlaan 200 D, B-3001 Leuven, Belgium

Abstract. We have analyzed quantization and confinement effects in nanostructured superconductors. Three different types of nanostructured samples were considered: individual structures (line, loop, dot), 1-dimensional (1D) clusters of loops and 2D clusters of antidots, and finally large lattices of antidots. Hereby, a crossover from individual elementary "plaquettes" (=dot, loop, etc.), via their clusters, to huge arrays of these elements, is realized. The main idea of our review was to investigate the effect of the boundary conditions on confinement of the superconducting condensate and the vortices, by taking samples of different topology and, through that, modifying the lowest Landau level $E_{LLL}(H)$. Since the critical temperature versus applied magnetic field $T_c(H)$ is, in fact, $E_{LLL}(H)$ measured in temperature units, it is varied as well when the sample topology is changed through nanostructuring. We demonstrate that in all considered nanostructured superconductors the shape of the $T_c(H)$ phase boundary is determined by the confinement topology in a unique way.

Lateral nanostructuring can also be efficiently used to control flux confinement phenomena. This will be illustrated by considering pinning phenomena in superconductors with regular arrays of microholes ("antidot lattices").

Optimizing, for the same material, the confinement topology for the superconducting condensate and for the penetrating magnetic flux, two important critical parameters, $T_c(H)$ and the critical current $j_c(H)$ can be increased up to their theoretical limits.

[1)] Short version of the book chapter in 'Handbook of Nanostructured Materials and Nanotechnology', Vol. 3, Chap. 9, p. 451-525, eds. H. S. Nalwa, Academic Press, San Diego, 1999.

I INTRODUCTION

A Quantization and confinement

"Confinement" and "quantization" are two closely related definitions: if a particle is "confined" then its energy is "quantized", and vice versa. According to the dictionary, to "confine" means to "restrict within limits", to "enclose", and even to "imprison". A typical example, illustrating the relation between confinement and quantization, is the restriction of the motion of a particle by enclosing it within an infinite potential well of size L_A. Due to the presence of an infinite potential $U(x)$ (Fig. 1) for $x < 0$ and $x > L_A$, the wave function $\Psi(x)$ describing the particle is zero outside the well: $\Psi = 0$ for $x < 0$ and $x > L_A$ and, in the region with $U(x) = 0$ $(0 \leq x \leq L_A)$, the solutions of the one-dimensional Schrödinger equation correspond to standing waves with an integer number n of half wavelengths λ along $L_A : n\,\lambda_n/2 = L_A$.

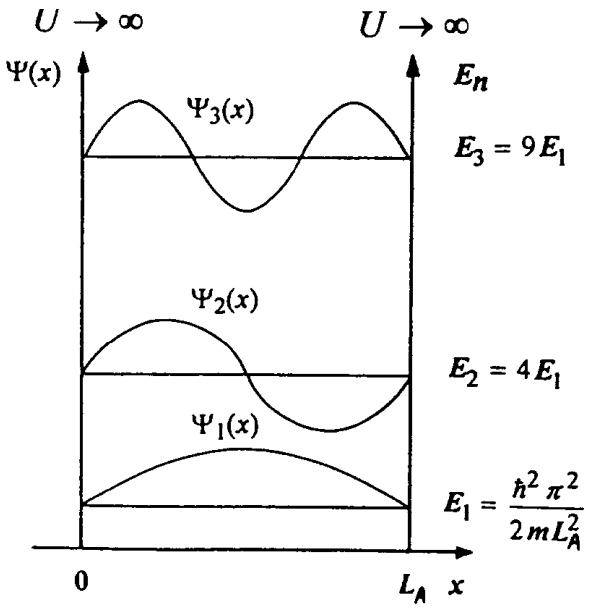

FIGURE 1. Confinement and quantization of the motion of a particle by an infinite potential well applied on the length scale L_A for $n = 1$, 2 and 3. (adapted from Ref. [1])

This simple constraint results in the well-known quantized energy spectrum

$$E_n = \frac{\hbar^2 k_n^2}{2m} = \frac{\hbar^2 (2\pi/\lambda_n)^2}{2m} = \frac{\hbar^2 \pi^2}{2mL_A^2} n^2 \qquad (1)$$

Here k_n is the wave number and m is the free electron mass. To have an idea about the characteristic energy scales involved and their dependence upon the

confinement length L_A, the energies E_1 (Eq. (1)) for electrons confined by an infinite potential well with the sizes 1 Å, 1 nm and 1 μm, are given in Table 1.

TABLE 1. Confinement by the infinite potential well

Confinement length L_A	Energy E_1	Temperature T
1 Å	$40\,eV$	$4 \times 10^5\,K$
1 nm	$0.4\,eV$	$4 \times 10^3\,K$
1 μm	$0.4\,\mu eV$	4 mK

B Nanostructuring

Recent impressive progress in nanofabrication has made it possible to realize the whole range of confinement lengths L_A : from 1 μm (photo-and e-beam lithography), via 1 nm to 1 Å (single atom manipulation) and, through that, to control the confinement energy (temperature) from a few mK higher up to far above room temperature (Table 1).

This progress has stimulated dramatically the experimental and theoretical studies of different nanostructured materials and individual nanostructures. The interest towards such structures arizes from the remarkable principle of "quantum design", when quantum mechanics can be efficiently used to tailor the physical properties of nanostructured materials.

Nanostructuring can also be considered as a sort of artificial modulation. We can identify then the main classes of nanostructured materials using the idea of their modification along one-, two- or three-axes, thus introducing 1-dimensional (1D)-, 2D- or 3D- artificial modulation (Fig. 2).

The 1D or "vertical" modulation represents then the class of superlattices or multilayers (Fig. 2a) formed by alternating individual films of two (A, B) or more different materials in a stack. Some examples of different types of multilayers are superconductor/insulator (Pb/Ge, WGe/Ge,...), superconductor/metal (V/Ag,...), superconductor/ferromagnet (Nb/Fe, V/Fe,...), ferromagnet/metal (Fe/Cr, Cu/Co,...), etc. [2–13].

The "horizontal" (lateral) superlattices (Fig. 2b) correspond to the 2D artificial modulation achieved by a lateral repetition of one (A), two (A,B) or more elements (further on we shall call them "elementary plaquettes"). As examples, we should mention here antidot arrays or antidot lattices, when A=microhole ("antidot"), or arrays and lateral superlattices consisting of magnetic dots.

If the 2D lateral modulation is applied to each individual layer of a multilayer or superlattice, then we deal with the 1D+2D=3D artificial modulation (Fig. 2c). For example, if arrays of antidots are made in a multilayer, then

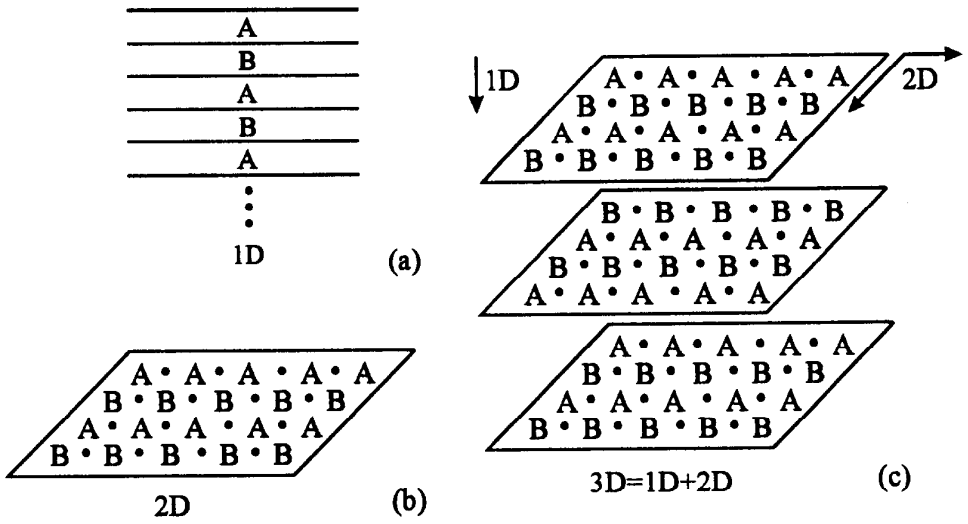

FIGURE 2. Schematic presentation of the vertical modulation in superlattices or multilayers (a), of the horizontal modulation achieved by a lateral repetition of elements A and B (b) and of the 1D+2D=3D artificial modulation (c). (adapted from Ref. [1])

we have a system with 3D artificial modulation which combines 2D lateral "horizontal" with the 1D "vertical" modulation.

Finally, macroscopic nanostructured samples, with a huge number N of repeated elementary nanoplaquettes (A,B,...), are examples of very complicated systems if the confined charge carriers or flux lines are strongly interacting with each other and the relevant interaction is of a long range. In this case the essential physics of such systems can be understood much better if one uses *clusters* of elements ($N \simeq 10$), instead of their *huge arrays* ($N \to \infty$) (Fig. 3). Schematic presentation of the vertical modulation in superlattices or multilayers (a), of the horizontal modulation achieved by a lateral repetition of elements A and B (b) and of the 1D+2D=3D artificial modulation (c). (adapted from Ref. [1])

These clusters, occupying an intermediate place between individual nanostructures ($N = 1$) and nanostructured materials ($N \to \infty$), are very helpful model objects to study the interactions between flux lines or charge carriers confined by finite arrays (clusters) of elements A. The "growth" of clusters on the way from an individual object A to a huge array of A's can be done either in a 1D or 2D fashion (Fig. 3), thus realizing 1D chains or 2D-like clusters of elements A.

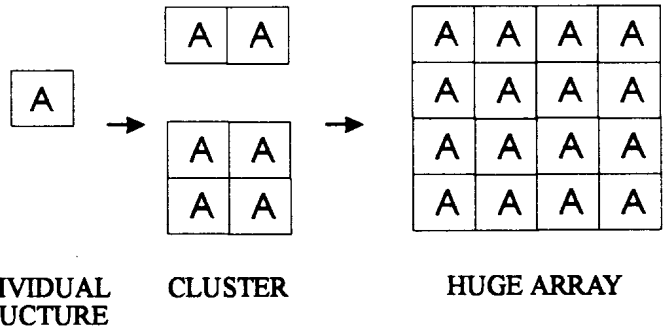

FIGURE 3. Schematic presentation of an individual structure (A="nanoplaquette"), a cluster of nanoplaquettes and a huge array of nanoplaquettes. (adapted from Ref. [1])

C Confining the superconducting condensate

The nanostructured materials and individual nanostructures, introduced in the previous section, can be prepared using modern facilities for nanofabrication. It is worth, however, first asking ourselves a few simple questions like: *why it is important to make such structures, what interesting new physics should be expected, and why it is of interest to focus on superconducting (and not, for example, normal metallic) nanostructured materials?*

First of all, by making nanostructured materials, one creates an *artificial potential* in which charge carriers or flux lines are confined. The size L_A of an elementary "plaquette" A, gives roughly the expected energy scale in accordance with Table 1, while the positions and topology of the elements A determine the pattern of the potential modulation. The concentration of charge carriers or flux lines can be controlled by varying a gate voltage (in 2D electron gas systems) [14] or the applied magnetic field (in superconductors) [15]. In this situation, different commensurability effects between the fixed number of elements A in an array and a tunable number of charge or flux carriers are observed.

Secondly, modifying the sample topology in nanostructured materials creates a *unique possibility to impose the desired boundary conditions*, and through that to change the properties of the sample. A Fermi liquid or a superconducting condensate confined within such materials will be subjected to severe constraints and, as a result, the properties of these materials will be strongly affected by the boundary conditions.

While a normal metallic system should be considered quantum-mechanically by solving the Schrödinger equation:

$$\frac{1}{2m}\left(-\imath\hbar\vec{\nabla} - e\vec{A}\right)^2 \Psi + U\,\Psi = E\,\Psi\,, \tag{2}$$

a superconducting system is described by the two coupled Ginzburg-Landau

(GL) equations:

$$\frac{1}{2m^\star}(-i\hbar\vec{\nabla} - e^\star\vec{A})^2\Psi_s + \beta|\Psi_s|^2\Psi_s = -\alpha\Psi_s \tag{3}$$

$$\vec{j} = \vec{\nabla}\times\vec{h} = \frac{e^\star}{2m^\star}\left[\Psi_s^\star(-i\hbar\vec{\nabla} - e^\star\vec{A})\Psi_s + \Psi_s(i\hbar\vec{\nabla} - e^\star\vec{A})\Psi_s^\star\right] , \tag{4}$$

with $\vec{A}$ the vector potential which corresponds to the microscopic field $\vec{h} = rot\vec{A}/\mu_0$, U the potential energy, E the total energy, α a temperature dependent parameter changing sign from $\alpha > 0$ to $\alpha < 0$ as T is decreased through T_c, β a positive temperature independent constant, $m^\star$ the effective mass which can be chosen arbitrarily and is generally taken as twice the free electron mass m.

Note that the first GL equation (Eq. (3)), with the nonlinear term $\beta|\Psi_s|^2\Psi_s$ neglected, is the analogue of the Schrödinger equation (Eq. (2)) with $U = 0$, when making a few substitutions: $\Psi_s \leftrightarrow \Psi$, $e^\star \leftrightarrow e$, $-\alpha \leftrightarrow E$ and $m^\star \leftrightarrow m$. The superconducting order parameter Ψ_s corresponds to the wave function Ψ in Eq. (2). The effective charge $e^\star$ in the GL equations is $2e$, i.e. the charge of a Cooper pair, while the temperature dependent GL parameter α

$$-\alpha = \frac{\hbar^2}{2m^\star\,\xi^2(T)} \tag{5}$$

plays the role of E in Schrödinger equation. Here $\xi(T)$ is the temperature dependent coherence length:

$$\xi(T) = \frac{\xi(0)}{\sqrt{1-\frac{T}{T_{c0}}}}. \tag{6}$$

Schematic presentation of an individual structure (A="nanoplaquette"), a cluster of nanoplaquettes and a huge array of nanoplaquettes. (adapted from Ref. [1])

The boundary conditions for interfaces normal metal-vacuum and superconductor-vacuum are, however, different (Fig. 4):

$$\Psi\Psi^\star|_b = 0 \tag{7}$$

$$(-i\hbar\vec{\nabla} - e^\star\vec{A})\Psi_s\Big|_{\perp,b} = 0 \tag{8}$$

i.e. for normal metallic systems *the density* is zero (Dirichlet boundary condition), while for superconducting systems, *the gradient* of Ψ_s (Neumann boundary condition) has no component perpendicular to the boundary. As a consequence, the supercurrent cannot flow through the boundary. The nucleation

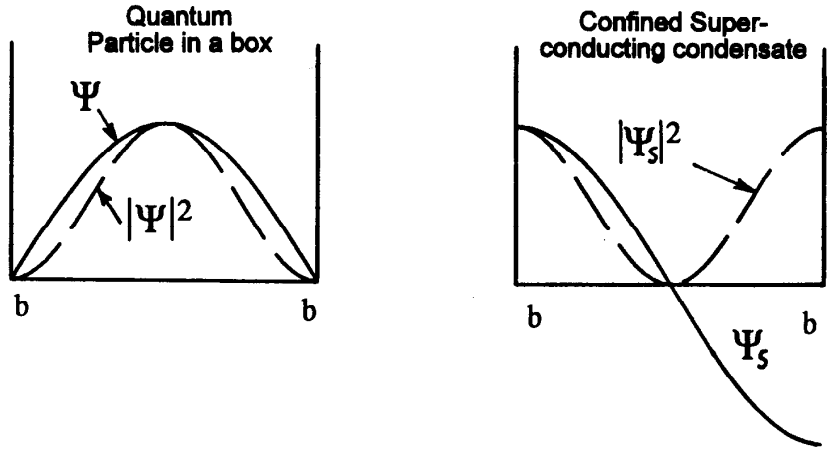

FIGURE 4. Boundary conditions for interfaces normal metal-vacuum (quantum particle in a box) and superconductor-vacuum (confined superconducting condensate). (adapted from Ref. [1])

of the superconducting condensate is favored at the superconductor/ vacuum interfaces, thus leading to the appearance of superconductivity, at the third critical field $H_{c3}(T)$, in a surface sheet with a thickness $\xi(T)$ (Fig. 5).

For bulk superconductors the surface-to-volume ratio is negligible and therefore superconductivity in the bulk is not affected by a thin superconducting surface layer. For nanostructured superconductors with antidot arrays, however, the boundary conditions (Eq. (8)) and the surface superconductivity introduced through them, become very important if $L_A \leq \xi(T)$. The advantage of superconducting materials in this case is that it is not even necessary to go to nm scale (like for normal metals), since for L_A of the order of 0.1-1.0 μm the temperature range where $L_A \leq \xi(T)$, spreads over $0.01 - 0.1$ K below T_c due to the divergence of $\xi(T)$ at $T \to T_{c0}$ (Eq. (6)).

In principle, the mesoscopic regime $L_A \leq \xi(T)$ (and $L_A \leq \lambda(T)$, with λ the magnetic penetration depth) can eventually be reached even in bulk superconducting samples with $L_A \sim 1$ cm-1 m, since $\xi(T)$ (and $\lambda(T)$ as well) diverges at $T \to T_{c0}$. However, the temperature window where $L_A \leq \xi(T)$ is so narrow, not more than ~ 1 nK below T_{c0}, that one needs ideal sample homogeneity and perfect temperature stability.

In the mesoscopic regime $L_A \leq \xi(T)$, which is quite easily realized in nanostructured materials, the surface superconductivity can cover the whole available space occupied by the material, thus spreading superconductivity all over the sample. It is then evident that in this case the surface effects play the role of bulk effects (see Fig. 5).

Using the similarity between the linearized GL equation (Eq. (3)) and the Schrödinger equation (Eq. (2)), the approach to determine $T_c(H)$ can be

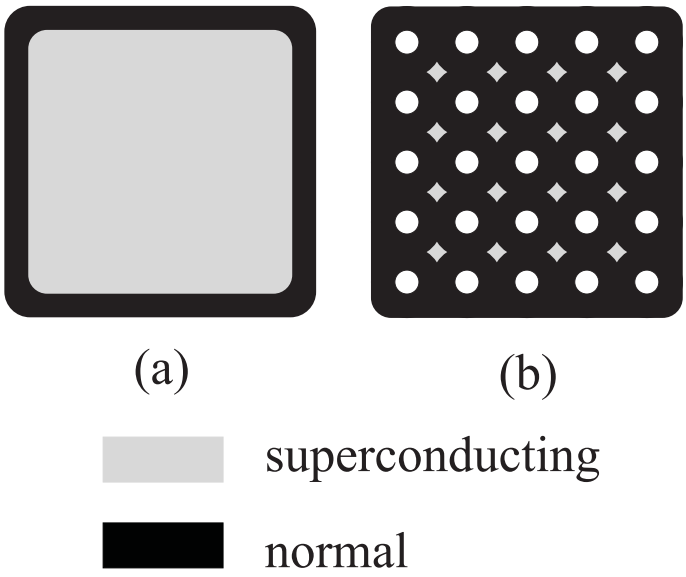

FIGURE 5. Schematic illustration of the surface superconductivity nucleated at the third critical field $H_{c3}(T)$. (a) In a bulk superconductor the surface superconducting sheet appears only at the external sample boundary, (b) while in a laterally nanostructured superconductor the surface superconductivity appears around each antidot, thus covering the whole sample interior. In the latter case the role of $H_{c2}(T)$ is played by $H_{c3}(T)$.

formalized as follows: since the parameter -α (Eqs. (3) and (5)) plays the role of energy E (Eq. (2)), then *the highest possible temperature $T_c(H)$ for the nucleation of the superconducting state in presence of the magnetic field H always corresponds to the lowest Landau level $E_{LLL}(H)$ found by solving the Schrödinger equation (Eq. (2)) with "superconducting" boundary conditions (Eq. (8)).*

Figure 6 illustrates the application of this basic rule to the calculation of the upper critical field $H_{c2}(T)$: indeed, if the well-known classical Landau solution for the lowest level in a bulk sample $E_{LLL}(H) = \hbar\omega/2$, where $\omega = e^\star \mu_0 H/m^\star$ is the cyclotron frequency, is taken, then, from -$\alpha = E_{LLL}(H)$, we have

$$\frac{\hbar^2}{2m^\star\,\xi^2(T)} = \left.\frac{\hbar\omega}{2}\right|_{H=H_{c2}} \tag{9}$$

with the help of Eq. (5). We obtain:

$$\mu_0 H_{c2}(T) = \frac{\Phi_0}{2\pi\xi^2(T)}\,, \tag{10}$$

with $\Phi_0 = h/e^\star = h/2e$ the superconducting flux quantum.

In nanostructured superconductors, where the boundary conditions (Eq. (8)) strongly influence the Landau level scheme, $E_{LLL}(H)$ has to be

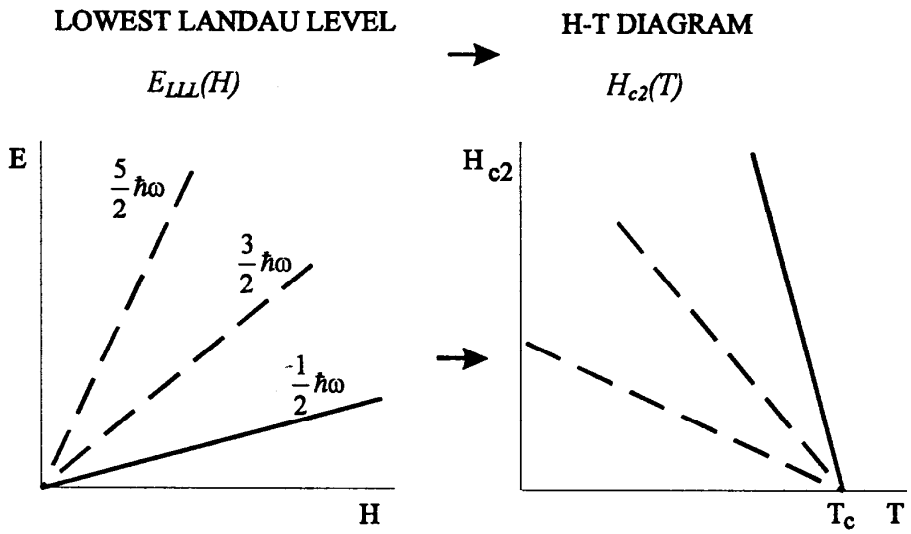

FIGURE 6. Landau level scheme for a particle in a magnetic field. From the lowest Landau level $E_{LLL}(H) = \hbar\omega/2$ the second critical field $H_{c2}(T)$ is derived (solid line). (adapted from Ref. [1])

calculated for each specific confinement geometry. By measuring the shift of the critical temperature $T_c(H)$ in a magnetic field, one can compare the experimental phase boundary $T_c(H)$ with the calculated level $E_{LLL}(H)$ and thus check the effect of the confinement topology on the superconducting phase boundary for a series of nanostructured superconducting samples. The transition between normal and superconducting states is usually very sharp and therefore the lowest Landau level can be easily traced as a function of applied magnetic field. The midpoint of the resistive transition from the superconducting to the normal state is usually taken as the criterion to determine $T_c(H)$. After the introduction, we are now ready to formulate the layout of this review article: we present the systematic analysis of the influence of the confinement geometry on the superconducting phase boundary $T_c(H)$ in a series of nanostructured samples. We start with individual nanostructures of different topologies (lines, loops, dots) (Section II) and then focus on "intermediate" systems: clusters of loops fabricated in the form of a 1D chain of loops (Section III.A) or 2D antidot clusters (Section III.B). Huge arrays of antidots are considered in Section IV where we deal, first of all, with the $T_c(H)$ boundary for superconducting films with antidot lattices. We then briefly discuss flux confinement phenomena in superconductors with an antidot lattice.

II INDIVIDUAL NANOSTRUCTURES

To begin this section, we present the experimental results on the $T_c(H)$ phase boundary of individual superconducting mesoscopic structures of different topology. It is important to keep other parameters of these samples constant, like material from which they are made (Al), the width of the lines ($w = 0.15\,\mu$m) and the film thickness $\tau = 25$ nm the same for all three structures, thus directly relating the differences in $T_c(H)$ to topological effects. The magnetic field H is always applied perpendicular to the structures.

A Line

In Fig. 7a the phase boundary $T_c(H)$ of a mesoscopic line [16] is shown. The solid line gives the $T_c(H)$ calculated from the well-known formula [17]:

$$T_c(H) = T_{c0}\left[1 - \frac{\pi^2}{3}\left(\frac{w\,\xi(0)\mu_0 H}{\Phi_0}\right)^2\right] \tag{11}$$

which, in fact, describes the parabolic shape of $T_c(H)$ for a thin film of thickness w in parallel magnetic field. Since the cross-section, exposed to the applied magnetic field, is the same for a film of thickness w in a parallel magnetic field and for a mesoscopic line of width w in a perpendicular field, the same formula can be used for both [16]. Indeed, the solid line in Fig 7a is a parabolic fit of the experimental data with Eq. (11) where $\xi(0) = 110$ nm was obtained as a fitting parameter. The coherence length obtained using this method, coincides reasonably well with the dirty limit value $\xi(0) = 0.85(\xi_0\ell)^{1/2}$=132 nm calculated from the known BCS coherence length ξ_0=1600 nm for bulk Al [18] and the mean free path $\ell = 15$ nm, estimated from the normal state resistivity ρ at $4.2\,K$ [19].

Another simple argument can be used as well to explain the parabolic relation $T_c(H) \propto H^2$: the expansion of the energy $E(H)$ in powers of H, as given by the perturbation theory, is [20]:

$$E(H) = E_0 + A_1 L H + A_2 S_e H^2 + \cdots \tag{12}$$

where A_1 and A_2 are constant coefficients, the first term E_0 represents the energy levels in zero field, the second term is the linear field splitting with the orbital quantum number L and the third term is the diamagnetic shift, with S_e the area exposed to the applied magnetic field.

Now, for the topology of the line with a width w much smaller than the Larmor radius $r_H \gg w$, any orbital motion is impossible due to the constraints imposed by the boundaries onto the electrons inside the line. Therefore, in this particular case $L = 0$ and $E(H) = E_0 + A_2 S_e H^2$, which immediately leads to the parabolic relation $T_c \propto H^2$. This diamagnetic shift of $T_c(H)$ can be

understood in terms of a partial screening of the magnetic field H due to the non-zero width of the line [21].

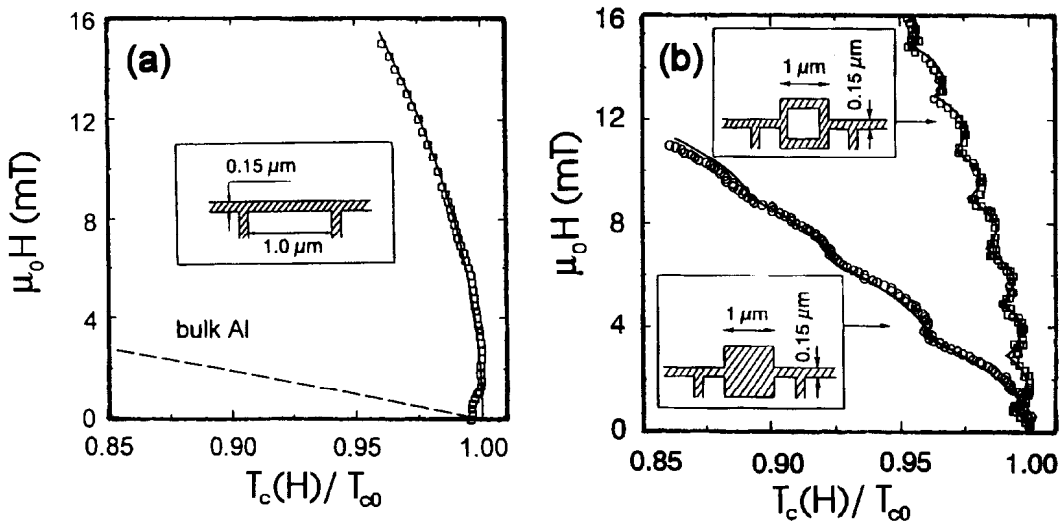

FIGURE 7. The measured superconducting/normal phase boundary as a function of the reduced temperature $T_c(H)/T_{c0}$ for a) the line, and b) the loop and the dot. The solid line in (a) is calculated using Eq. (11) with $\xi(0) = 110$ nm as a fitting parameter. The dashed line represents $T_c(H)$ for bulk Al. Comparing $T_c(H)$ for these three different mesoscopic structures, made of the same material, one clearly sees the effect of topology on $T_c(H)$. (adapted from Ref. [1])

B Loop

The $T_c(H)$ of the mesoscopic loop [16], shown in Fig. 7b, demonstrates very distinct Little-Parks (LP) oscillations [22] superimposed on a monotonic background. A closer investigation leads to the conclusion that this background is very well described by the same parabolic dependence as the one which we just discussed for the mesoscopic line [16] (see the solid line in Fig. 7a). As long as the width of the strips w, forming the loop, is much smaller than the loop size, the total shift of $T_c(H)$ can be written as the sum of an oscillatory part, and the monotonic background given by Eq. (11) [16,23]:

$$T_c(H) = T_{c0}\left[1 - \frac{\pi^2}{3}\left(\frac{w\,\xi(0)\mu_0 H}{\Phi_0}\right)^2 - \frac{\xi^2(0)}{R^2}\left(n - \frac{\Phi}{\Phi_0}\right)^2\right] \qquad (13)$$

where $R^2 = R_1\,R_2$ is the product of inner and outer loop radius, and the magnetic flux threading the loop $\Phi = \pi R^2 \mu_0 H$. The integer n has to be chosen so as to maximize $T_c(H)$ or, in other words, selecting $E_{LLL}(H)$.

The LP oscillations originate from the fluxoid quantization requirement, which states that the complex order parameter $\Psi_s = |\Psi_s| \exp(\imath\varphi)$ should be a single-valued function when integrating along a closed contour

$$\oint \vec{\nabla}\varphi \cdot dl = n\, 2\pi \qquad\qquad n = \cdots, -2, -1, 0, 1, 2, \cdots \tag{14}$$

Fluxoid quantization gives rise to a circulating supercurrent in the loop when $\Phi \neq n\Phi_0$, which is periodic with the applied flux Φ/Φ_0.

Using the sample dimensions and the value for $\xi(0)$ obtained before for the mesoscopic line (with the same width $w = 0.15\ \mu$m), the $T_c(H)$ for the loop can be calculated from Eq. (13) without any free parameter. The solid line in Fig. 7b shows indeed a very good agreement with the experimental data [16]. It is worth noting here that the amplitude of the LP oscillations is about a few mK - in qualitative agreement with the simple estimate given in Table 1 for $L_A \simeq 1\ \mu$m.

The susceptibility of a single mesoscopic Al ring, showing LP oscillations, has been studied recently by Zhang and Price [24], who found an excellent agreement with the GL theory for the susceptibility below T_c.

The lower critical field of a loop is found from the condition that half a flux quantum is applied, thus giving [25]:

$$\mu_0 H_{c1}^{loop} = \frac{1}{2}\frac{\Phi_0}{\pi R^2}\,, \tag{15}$$

which is totally different from the H_{c1} value of a bulk superconductor.

In order to measure the resistance of a mesoscopic loop, electrical contacts have, of course, to be attached to it, and as a consequence, the confinement geometry is changed. A loop with attached contacts and the same loop without any contacts are, strictly speaking, different mesoscopic systems. This "disturbing" or "invasive" aspect ("Schrödinger cat") of probing a quantum object can now be exploited for the study of nonlocal effects [26]. Due to the divergence of the coherence length $\xi(T)$ at $T = T_{c0}$ (Eq. (6)) the coupling of the loop with the attached leads is expected to be very strong for $T \to T_{c0}$.

The measured superconducting/normal phase boundary as a function of the reduced temperature $T_c(H)/T_{c0}$ for a) the line, and b) the loop and the dot. The solid line in (a) is calculated using Eq. (11) with $\xi(0) = 110$ nm as a fitting parameter. The dashed line represents $T_c(H)$ for bulk Al. Comparing $T_c(H)$ for these three different mesoscopic structures, made of the same material, one clearly sees the effect of topology on $T_c(H)$. (adapted from Ref. [1])

Fig. 8 shows the results of these measurements [26]. Both "local" (potential probes across the loop V_1/V_2) and "nonlocal" (potential probes aside of the loop V_1/V_3 or V_2/V_4) LP oscillations are clearly observed. For the "local" probes there is an unexpected and pronounced increase of the oscillation amplitude with increasing field, in disagreement with previous measurements on

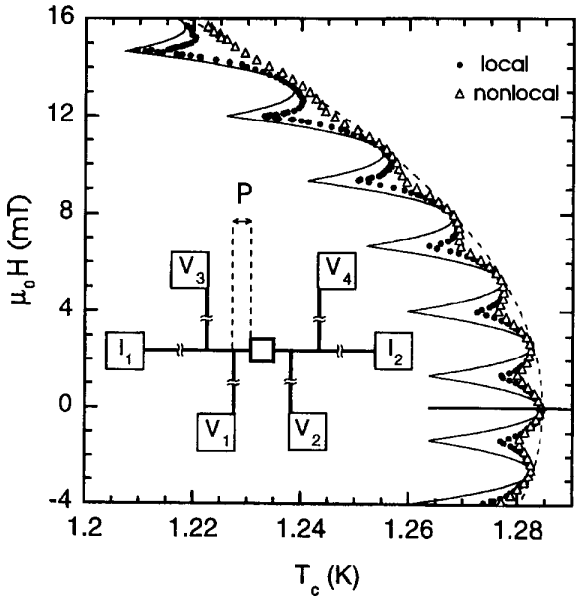

FIGURE 8. Local (V_1/V_2) and nonlocal (V_1/V_3 or V_2/V_4) phase boundaries $T_c(H)$. The measuring current is sent through I_1/I_2. The solid and dashed lines correspond to the theoretical $T_c(H)$ of an isolated loop and a one-dimensional line, respectively, both made of strips of width w. The inset shows a schematic of the structure, where the distance $P = 0.4\,\mu$m. (adapted from Ref. [26])

Al microcylinders [23]. In contrast to this, for the "nonlocal" LP effect, the oscillations rapidly vanish when the magnetic field is increased.

When increasing the field, the background suppression of T_c (Eq. (11)) results in a decrease of $\xi(T)$. Hence, the change of the oscillation amplitude with H is directly related to the temperature-dependent coherence length. As long as the coherence of the superconducting condensate protuberates over the nonlocal voltage probes, the nonlocal LP oscillations can be observed.

On the other hand, the importance of an "arm" attached to a mesoscopic loop, was already demonstrated theoretically by de Gennes in 1981 [27]. For a perfect 1D loop (vanishing width of the strips) adding an "arm" will result in a decrease of the LP oscillation amplitude, what was observed indeed at low magnetic fields, where $\xi(T)$ is still large. With these experiments, it has been proved that adding probes to a structure considerably changes both the confinement topology and the phase boundary $T_c(H)$.

The effect of topology on $T_c(H)$, related to the presence of the sharp corners in a square loop, has been considered by Fomin *et al.* [28]. In the vicinity of the corners the superconducting condensate sustains a higher applied magnetic field, since at these locations the superfluid velocity is reduced, in comparison with the ring. Consequently, in a field-cooled experiment, superconductivity

will nucleate first around the corners [28]. Eventually, for a square loop, the introduction of a *local* superconducting transition temperature seems to be needed. As a result of the presence of the corner, the $H_{c3}(T)$ of a wedge with an angle θ [29] will be strongly enhanced at the corner resulting in the ratio $H_{c3}/H_{c2} \approx 3.79$ for $\theta \approx 0.44\,\pi$ [29].

Another interesting possibility for a superconducting ring has been analyzed in Refs. [30–34]: under certain conditions superconductivity spontaneously breaks at some spot along the perimeter of the ring, so that the *superconducting area changes from multiple to single connectivity.* The physics behind this interesting theoretical prediction is the following. The oscillatory $T_c(\Phi)$ phase boundary is caused by a periodic variation of a circular supercurrent (when the applied flux Φ/Φ_0 is not integer, see Fig. 9a) which is induced in a ring in order to fulfill fluxoid quantization. The highest current (and therefore the strongest reduction of $T_c(\Phi)$ is realized for half integer flux when $\Phi/\Phi_0 - n = 1/2$ (see Fig. 7b and 8). In this situation it may turn out, however, that somewhere in the ring the order parameter Ψ_s is spontaneously suppressed and a sort of 'normal core' is created somewhere along the ring circumference (see Fig. 9b). The energy of this normal state core, below the $T_c(\Phi)$ line, is, of course, higher than the energy corresponding to a superconducting state everywhere in the ring, but, at the expense of that, the circular supercurrent is interrupted, thus effectively opening the ring for entrance and removal of flux. While Horane *et al.* [30] predicted the existence of the singly connected state for rings made of "1D" strips, Berger and Rubinstein [33] showed that the temperature region where the singly connected state exists, can be enhanced by proper tuning the nonuniform 'strip width' profiles along the ring.

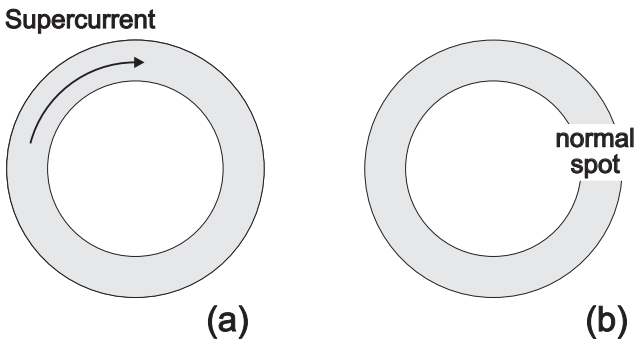

FIGURE 9. Schematic view of a mesoscopic loop in (a) the multiply connected state, (b) the singly connected state, where a normal spot is spontaneously created and consequently no supercurrent flows.

C Dot

For a cylindrical symmetry, the choice of the coordinates (r, φ, z) and the gauge $\vec{A} = (Hr/2)\,\vec{e}_\varphi$, where $\vec{e}_\varphi$ is the tangential unit vector, is well suited. The solution of the Hamiltonian (Eq. (3) with the nonlinear term neglected) in cylindrical coordinates has the following form [35]:

$$\Psi_s(r,\varphi) = e^{\pm \imath L\varphi} r^L \gamma^{(L+1)/2} \exp\left(-\frac{\gamma r^2}{2}\right) M(-N, L+1, \gamma r^2)\,. \tag{16}$$

Here $\gamma = e^\star\,\mu_0 H/h$ and the energy $E_\perp$ of the motion in the plane perpendicular to H is determined by the orbital quantum number L and parameter N, which is not necessarily an integer number, as we shall see later:

$$E_\perp = \frac{e^\star \hbar\,\mu_0 H}{2\,m^\star}\,(2N \pm L + L + 1)\ . \tag{17}$$

The function M is the Kummer function defined as:

$$M(a,c,y) = 1 + \frac{a}{c}y + \frac{a(a+1)}{c(c+1)}\frac{y^2}{2!} + \frac{a(a+1)(a+2)}{c(c+1)(c+2)}\frac{y^3}{3!} + \cdots, \tag{18}$$

where $a = -N$, $c = L+1$, $y = \gamma r^2$. Introducing the dimensionless radius $R = \sqrt{\gamma\, r^2} = \Phi/\Phi_0$, the superconducting order parameter can be written in the form

$$\Psi_L(R,\varphi) = e^{\pm \imath L\varphi} R^L \exp\left(-\frac{R^2}{2}\right) M(-N, L+1, R^2)\,. \tag{19}$$

The representation of the order parameter $\Psi_s = \sum_L c_L \Psi_L$ as an expansion over states with different L for infinite samples has been analyzed in Ref. [36], where $M(0, L+1, R^2) = 1$ has been taken. Under these conditions, the functions $|\Psi_L|$ have their maxima at $R^2 = L$, i.e., the area enclosed by the circle with the radius corresponding to the $|\Psi_L|$ maximum is always penetrated by an integer number L of the flux quanta: $\Phi/\Phi_0 = L$. Here in this review, we shall analyze the case of *finite* samples, where the N value has to be found from the boundary condition (Eq. (8)). It is very important to note that in the general form (Eq. (16) and Eq. (17)) there are no limitations on the parameter N: it is not necessarily an integer number. The only argument, which is usually given in favor of taking integer N, is a possibility to get a cut off in the summation (Eq. (18)). Indeed, if one inserts an integer N into the summation, then by adding 1 to N in each new term one eventually comes to the situation where $-N + N = 0$ and all subsequent terms in the summation will be equal to zero. Thus by the cutoff we just use a finite number of terms in the summation (Eq. (18)) and of course M is finite in this case. But we should keep in mind that any converging, but infinite row also gives a finite

solution for M. Therefore, not only positive integer N in Eq. (17), but also noninteger and even negative N values are possible. In finite size samples the N value, which we further denote as $N(L, R_0)$, has to be found from the boundary condition at $R = R_0$ (Eq. (8)), where R_0 is the normalized disk radius:

$$\left.\frac{\partial|\Psi_s(R)|}{\partial R}\right|_{R=R_0} . \tag{20}$$

Since we are looking for the lowest possible energy state, we should take the minus sign in the argument of the exponent $\exp(-\imath L\varphi)$ in the solution given by Eq. (18). In this case $-L$ and $+L$ in Eq. (17) cancel and for any L the energy levels are given by:

$$E_\perp = \hbar\omega\left(N + \frac{1}{2}\right) , \tag{21}$$

where $\omega = e^\star\mu_0 H/m^\star$ is the cyclotron frequency.

This result coincides with the well-known Landau quantization, but now N is *any real number, including negative real number*, which is to be calculated from Eq. (20). Using the expression

$$\frac{dM(a,c,y)}{dy} = \frac{a}{c}M(a+1, c+1, y) \tag{22}$$

for the derivative of the Kummer function, we can find the $N(L, R_0)$ value, which obeys the boundary condition (Eq. (20)), from the equation:

$$(L - R_0^2)M(-N, L+1, R_0^2) - \frac{2NR_0^2}{L+1}M(-N+1, L+2, R_0^2) = 0. \tag{23}$$

The remarkable thing about the $N(L, R_0)$ values, found from the solutions of Eq. (20), is that they are negative, which immediately gives the energy $E_\perp$ in Eq. (21) lower than $\hbar\omega/2$. *As a result of the confinement with the superconducting boundary conditions, the energy levels in finite samples lie below the classical value $\hbar\omega/2$ for infinite samples* [37]. The whole energy level scheme (Fig. 10), found by Saint-James [37], can be reconstructed by calculating $E_\perp$ vs. R_0^2 for different L values. From this diagram one can easily go to the field versus temperature plot, using the relation $E_\perp = -\alpha$.

To conclude this discussion, we note that in finite samples N is a bad quantum number. It is rather a parameter which has to be found from the boundary condition. A good quantum number for the problem is L. By forming a superconducting condensate with a proper finite L and $N(L, R_0) < 0$ we conserve the rotational momentum and at the same time reduce the energy below $\hbar\omega/2$ [38].

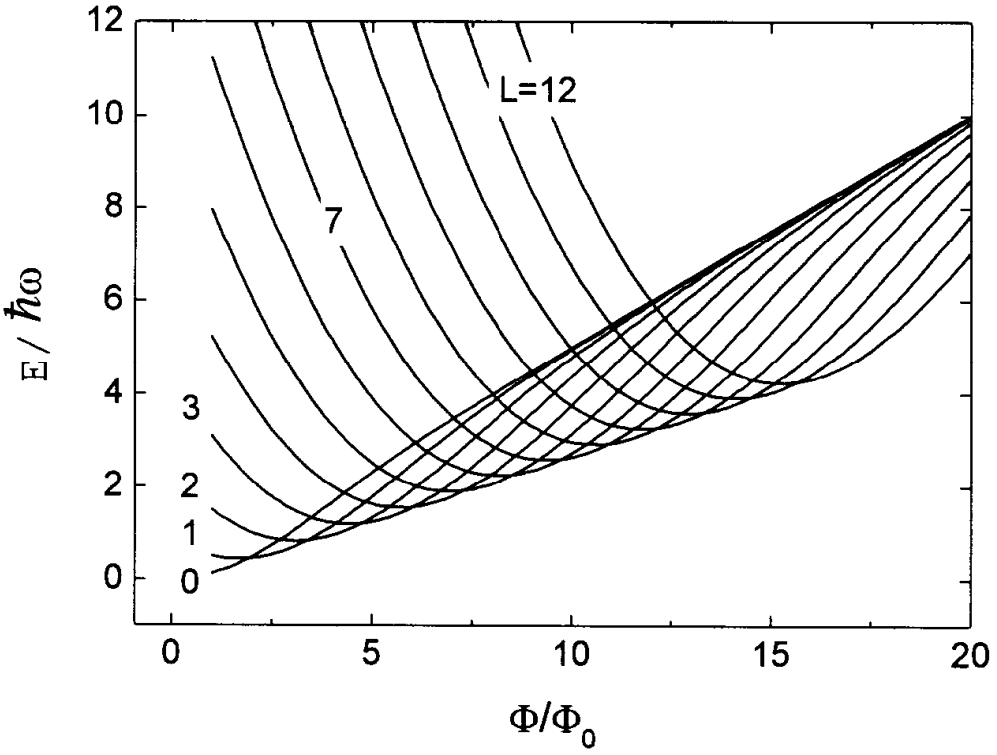

FIGURE 10. Energy levels versus normalized flux Φ/Φ_0 for a superconducting cylinder in a parallel magnetic field. The lowest lying cusplike $H_{c3}(T)$ line is formed due to the change of the orbital quantum number L. (adapted from Ref. [38])

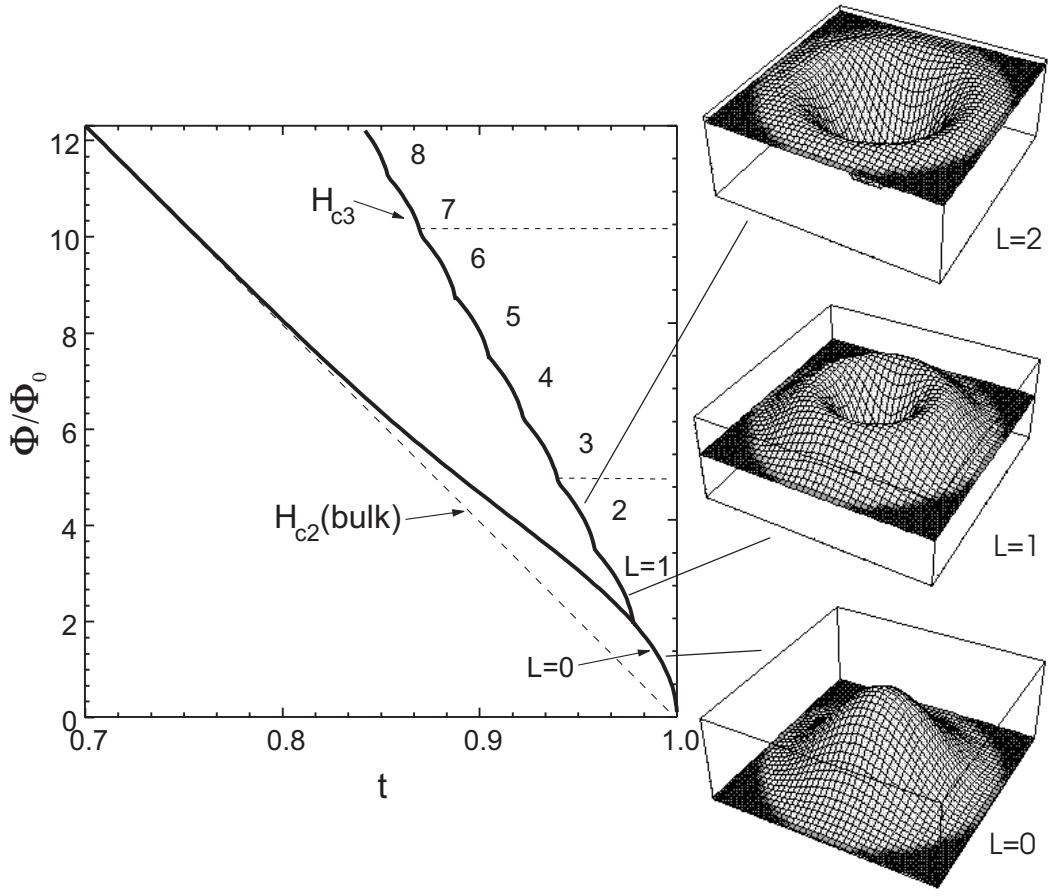

FIGURE 11. Third critical field H_{c3} (theory) and the bulk upper critical field H_{c2} (dashed line) vs. normalized temperature $t = T/T_{c0}$ for a superconducting disk. The cusplike $H_{c3}(T)$ line is formed due to the change of the orbital quantum number L. In the three-dimensional plots, $|\Psi|$ is depicted as a function of the spatial coordinates for several L values. (adapted

As shown above, because of the onset of surface superconductivity at $H_{c3}(T)$, corresponding to negative N in Eq. (21), the superconductivity can appear at magnetic fields well above the $H_{c2}(T)$ line (found for $N = 0$). By changing the variable $E_\perp$ in Fig. 10 into T, we obtain the cusplike phase boundary $H_{c3}(T)$ as shown in Fig. 11, which is due to switching between different orbital momenta L. The phase boundary of the superconducting disk (Fig. 11) has been observed experimentally by Buisson *et al.* [37] and by Moshchalkov *et al.* [16]. It should be emphasized here that the presence of the oscillations in the $H_{c3}(T)$ curve is crucially dependent on the imposed Neumann boundary conditions [25]. Contrary to that, the equivalent eigenvalue spectrum with Dirichlet boundary conditions does not show any oscillations, if one follows the lowest Landau level $E_{LLL}(H)$ [39].

The Landau level scheme for a cylindrical dot with "superconducting" boundary conditions (Eq. (8)) is presented in Fig. 10. Each level is characterized by a certain orbital quantum number L where $\Psi_s = |\Psi_s| \exp(\mp \imath L \varphi)$ [38]. The levels, corresponding to the sign "+" in the argument of the exponent are not shown since they are situated at energies higher than the ones with the sign "-". The lowest Landau level in Fig. 10 represents, in fact, a cusplike envelope, obtained from the switching between different L values with changing magnetic field. Following our main guideline that $E_{LLL}(H)$ determines $T_c(H)$, for the dot, a cusplike superconducting phase boundary with nearly perfect linear background is expected. The measured phase boundary $T_c(H)$, shown in Fig. 7b, can be nicely fitted by the calculated one (Fig. 10), thus proving that $T_c(H)$ of a superconducting dot indeed consists of cusps with different L's [37]. Each fixed L describes a giant vortex state which carries L flux quanta Φ_0. The linear background of the $T_c(H)$ dependence is very close to the third critical field $H_{c3}(T) \simeq 1.69\, H_{c2}(T)$, which is obtained in the $L \to \infty$ limit [18,40]. Contrary to the loop, where the LP oscillations are perfectly periodic, the dot demonstrates a certain aperiodicity [41], in very good agreement with the theoretical calculations [25,37].

The lower critical field of a cylindrical dot H_{c1}^{dot} corresponds to the change of the orbital quantum number from $L = 0$ to $L = 1$, i.e. to the penetration of the first flux line [25]:

$$\mu_0 H_{c1}^{dot} = 1.924\, \frac{\Phi_0}{\pi R^2}\,. \tag{24}$$

For a long mesoscopic cylinder described above, demagnetization effects can be neglected. On the contrary, for a thin superconducting disk, these effects are quite essential [42–44]. For a mesoscopic disk, made of a Type-I superconductor, the phase transition between the superconducting and the normal state is of the second order if the expulsion of the magnetic field from the disk can be neglected, i.e. when the disk thickness is comparable with ξ and λ. When the disk thickness is larger than a certain critical value first order phase transitions should occur. The latter has been confirmed in

ballistic Hall magnetometry experiments on individual Al disks [45–47]. A series of first order transitions between states with different orbital quantum numbers L have been seen in magnetization curves $M(H)$ [45] in the field range corresponding to the crossover between the Meissner and the normal states. Besides the cusplike $H_{c3}(T)$ line, found earlier in transport measurements [16,37], transitions between the $L = 2$ and $L = 1$ states have been observed [45] by probing the superconducting state below the $T_c(H)$ line with Hall micromagnetometry. Still deeper in the superconducting area the recovery of the normal Φ_0-vortices and the decay of the giant vortex state might be expected [44]. The former has been considered in Ref. [48] in the London limit, by using the image method. Magnetization and stable vortex configurations have been recently analyzed in mesoscopic disks in Refs. [42–44].

III CLUSTERS OF LOOPS AND ANTIDOTS

A 1D Clusters of loops

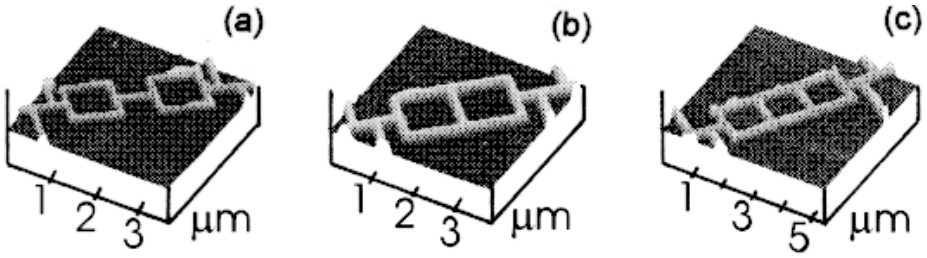

FIGURE 12. AFM micrographs of the studied structures: a) the bola, b) the double loop, and c) the triple loop. (adapted from Ref. [49])

After the description of the confinement effects of several individual superconducting structures (A = line, loop, dot) we are ready to move further on to clusters of elements A (Fig. 3) on our way from "single plaquette" samples to materials nanostructured by introducing huge arrays of plaquettes A. First we take A = loop and consider one-dimensional multiloop structures: "bola", double and triple loop Al structures. Figure 12 shows a AFM image of the structures. For these geometries some interesting theoretical predictions have been made, for which no experimental verification has been carried out up to now (see more in Ref. [49]). The loops in all three structures have the same dimensions, thus leading to the same magnetic field period $\mu_0 \Delta H = 1.24\, mT$. The strips forming the structures are 0.13 μm wide and the film thickness $\tau = 34$ nm. In all the experimental data shown here, the parabolic background (Eq. (11)) is already subtracted in order to allow a direct comparison with the theory. In the temperature interval where the $T_c(H)$ boundary was

measured, the coherence length $\xi(T)$ is considerably larger than the width w of the strips. This makes it possible to use the one-dimensional models for the calculation of $E_{LLL}(H)$ and thus $T_c(H)$. The basic idea is to consider $|\Psi_s|$ = constant across the strips forming the network and to allow a variation of $|\Psi_s|$ only along the strips. In the simplest approach $|\Psi_s|$ is assumed to be spatially constant (London limit) [50,51], in contrast to the de Gennes-Alexander (dGA) approach [67,27,52], where $|\Psi_s|$ is allowed to vary along the strips. In the latter approach one imposes:

$$\sum_n \left(\imath \frac{\partial}{\partial x} + \frac{2\pi}{\Phi_0} A_{\|}(x) \right) \Psi_s(x) = 0 \tag{25}$$

at the points where the current paths join. The summation is taken over all strips connected to the junction point. Here, x is the coordinate defining the position on the strips, and $A_{\|}$ is the component of the vector potential along x. Eq. (25) is often called the generalized first Kirchhoff law, ensuring current conservation [67]. The second Kirchhoff law for voltages in normal circuits is now replaced by the fluxoid quantization requirement (Eq. (14)), which should be fulfilled for each closed contour in the superconducting network (around each loop).

In Figs. 13-15 the $T_c(H)$ boundaries of the three structures are shown. The dashed lines are the phase boundaries calculated in the London limit, while the solid lines give the results from the dGA approach. As we discussed in Section II.B for a mesoscopic loop, attaching contacts modifies the confinement topology, so that the amplitude of the local LP oscillations is reduced at low magnetic fields. Here as well, the inclusion of the leads decreases the amplitude of the oscillations. The dash-dotted line in Figs. 13-15 gives the result of the dGA calculation where the presence of the leads has been included. The values for $\xi(0)$ obtained from the fits agree within a few percent with the $\xi(0)$ values found independently from the monotonic background of $T_c(\Phi)$ (see Eq. (11)).

First, in Fig. 13, we consider the mesoscopic "bola" - two loops connected by a wire. Fink *et al.* [67] showed that, in the complete magnetic flux interval, the spatially symmetric solution, with equal orientation of the supercurrents in both loops, has a lower energy than the antisymmetric solution. Coming back to the similarity between a mesoscopic loop and a hydrogen atom, we discussed in Section II.B, we can then compare the bola with a H_2 molecule, where the symmetric and the antisymmetric solutions correspond to singlet and triplet states, respectively. In fact, $T_c(\Phi)$ of the bola is the same as for a single loop provided that the length of the strip connecting the two loops is short, as confirmed by the LP oscillations observed in the experimental $T_c(\Phi)$ (Fig. 13).

In what follows we will focus on the results obtained by Bruyndoncx *et al.* [49] on the phase boundaries of the double (Fig. 14) and the triple loop (Fig. 15). To facilitate the discussion we divide the flux period in two intervals:

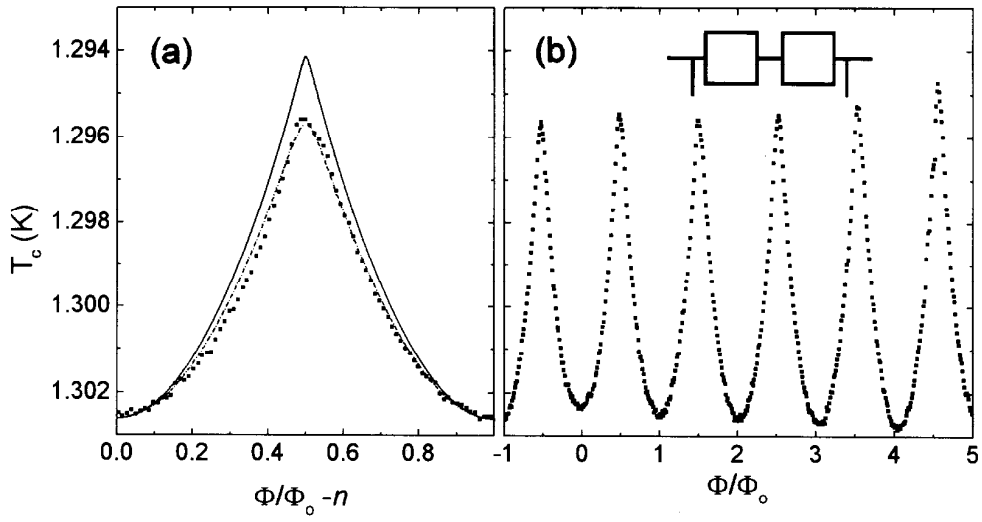

FIGURE 13. Experimental $T_c(\Phi)$ data for the **bola** with the parabolic background (Eq. (11)) subtracted. The dots are the experimental data points, while the lines correspond to the different theoretical results as explained in the text. a) Single period of $T_c(\Phi)$, b) A few periods of the experimental $T_c(\Phi)$ curve. (adapted from Ref. [1])

flux regime I for $\Phi/\Phi_0 < g$ or $\Phi/\Phi_0 > (1-g)$ and flux regime II for $g < \Phi/\Phi_0 < (1-g)$. In the flux regime I the phase boundaries, predicted by the different models, are nearly identical. Near $\Phi/\Phi_0 = 1/2$ (flux regime II), however, clear differences are found between the dGA approach and the London limit. The dGA result fits better the experimental data with respect to the crossover point g between regimes I and II, and the amplitude of the T_c oscillations. Using the dGA approach, the spatial modulation of $|\Psi_s|$ and the supercurrents for different values at the $T_c(\Phi)$ boundary has been calculated. In the flux regime I $|\Psi_s|$ varies only slightly and therefore the results of the London limit and the dGA models nearly coincide. The elementary loops have an equal fluxoid quantum number (and consequently an equal supercurrent orientation) for both the double and the triple loop geometry. For the double loop this leads to a cancellation of the supercurrent in the middle strip, while for the triple loop the fluxoid quantization condition (Eq. (14)) results in a different value for the supercurrent in the inner and the outer loops. As a result, the common strips of the triple loop structure carry a finite current.

In the flux regime II, qualitatively different states are obtained from the London limit and the dGA approach: the states calculated within the dGA approach have strongly modulated $|\Psi_s|$ along the strips. This is most severe for the double loop: Ψ_s shows a node ($|\Psi_s| = 0$) in the center of the common strip, the phase φ having a discontinuity of π at this point. This node is a one-dimensional analog of the core of an Abrikosov vortex, where the order

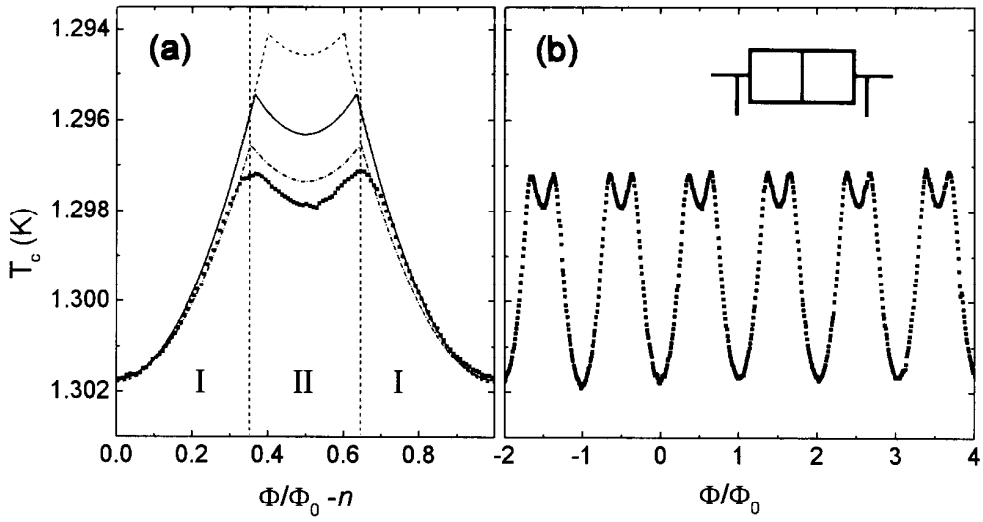

FIGURE 14. Experimental $T_c(\Phi)$ data for the **double loop** with the parabolic background (Eq. (11)) subtracted. The dots are the experimental data points, while the lines correspond to the different theoretical results as explained in the text. a) Single period of $T_c(\Phi)$, b) A few periods of the experimental $T_c(\Phi)$ curve. (adapted from Ref. [1])

parameter also vanishes and the phase shows a discontinuity. In Fig. 16 the spatial variation of $|\Psi_s|$ along the strips is shown for $\Phi/\Phi_0 = 0.36$ close to the crossover point g. The dashed curve gives $|\Psi_s|$ in flux regime I, which is quasi-constant. The strongly modulated solution, which goes through zero in the center, is indicated by the solid line. Although there exists a finite phase difference across the junction points of the middle strip, no supercurrent can flow through the strip due to the presence of the node. This node is predicted to persist when moving below the phase boundary into the superconducting state [53,54]. Already in 1964 Parks [55] anticipated that, in a double loop, "a part of the middle link will revert to the normal phase", and that "this in effect will convert the double loop to a single loop", giving an intuitive explanation for the maximum in $T_c(\Phi)$ at $\Phi/\Phi_0 = 1/2$. Such a modulation of $|\Psi_s|$ is obviously excluded in the London limit, where the loop currents have an opposite orientation and add up in the central strip, thus giving rise to a rather high kinetic energy. An extra argument in favor of the presence of the node is given by the much better agreement for the crossover point g when the presence of the leads is taken into account in the calculations (see dash-dotted line in Fig. 14).

For the triple loop (Fig. 15a) the modulation of $|\Psi_s|$ is still considerable in flux regime II, but it does not show any nodes. Therefore the supercurrent orientations can be found from the fluxoid quantum numbers $\{n_i\}$, obtained from integrating the phase gradients along each individual loop. When passing

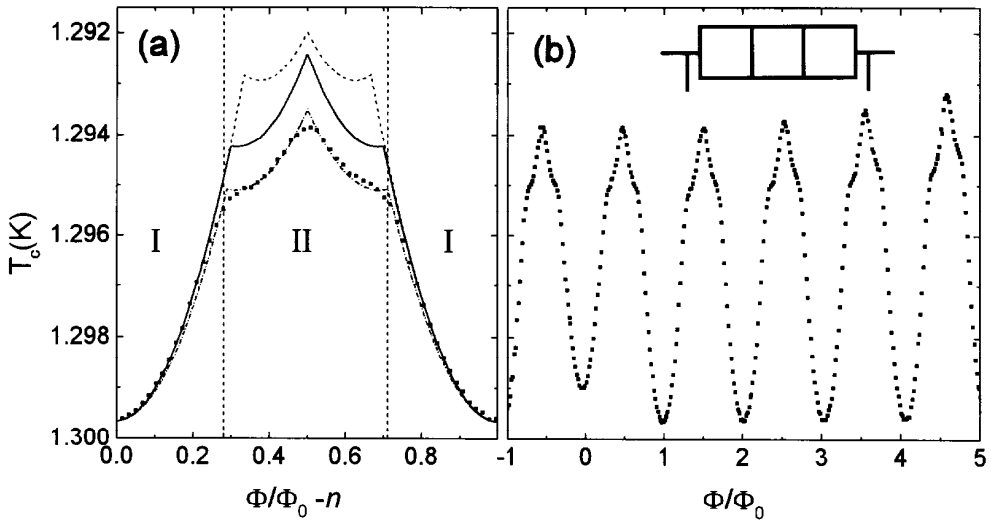

FIGURE 15. Experimental $T_c(\Phi)$ data for the **triple loop** with the parabolic background (Eq. (11)) subtracted. The dots are the experimental data points, while the lines correspond to the different theoretical results as explained in the text. a) Single period of $T_c(\Phi)$, b) A few periods of the experimental $T_c(\Phi)$ curve. (adapted from Ref. [1])

through the crossover point between flux regime I and regime II only the supercurrent in the middle loop is reversed, while increasing the flux above $\Phi/\Phi_0 = 1/2$ implies a reversal of the supercurrent in all loops.

Surprisingly, the behavior of a microladder with a linear arrangement of m loops appears to be *qualitatively different for even and for odd* m in the sense that m determines the presence or absence of nodes in the common strips. For an infinitely long microladder $|\Psi_s|$ was found to be spatially constant below a certain $\Phi < \Phi_c$ [56], which is analogous to the states in flux regime I. For fluxes $\Phi > \Phi_c$ modulated $|\Psi_s|$ states, with an incommensurate fluxoid pattern, were found. At $\Phi/\Phi_0 = 1/2$, nodes appear at the center of every second common (transverse) branch.

A variety of other structures (micronets) (coupled rings, bola's, a yin-yang, infinite microladders, bridge circuits, like a Wheatstone bridge, wires with dangling branches, etc.) formed by 1D wires, have been analyzed in a series of publications [27,53,54,56–67] using the approach, initiated in 1981 by de Gennes [27] and further developed by Alexander [52] and Fink *et al.* [67]. For all these structures very pronounced effects of topology on $T_c(\Phi)$ and critical current have been predicted.

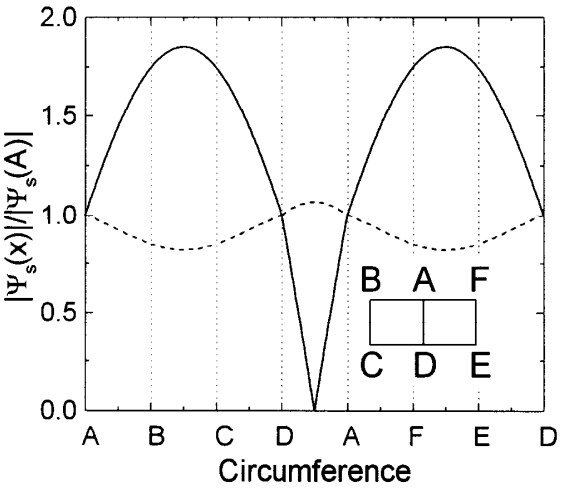

FIGURE 16. Calculated variation of $|\Psi_s|$ along the circumference of the double loop, at the phase boundary ($\Phi/\Phi_0 = 0.36$). The dashed line is the solution with $|\Psi_s|$ nearly spatially constant, while the solid line is the state with a node in the center of the strip connecting points A and D. (adapted from Ref. [1])

B 2D Clusters of antidots

As a 2D intermediate structure between individual elements A and their huge arrays (Fig. 3), we shall consider the superconducting microsquare with a 2×2 antidot cluster [68,69]. In this case, the symbol A from Figure 2 indicates an "antidot".

This microsquare with the 2×2 antidot cluster consists of a 2×2 μm^2 superconducting square with four antidots (i.e. square holes of 0.53 × 0.53 μm^2). A Pb/Cu bilayer with 50 nm of Pb and 17 nm of Cu was used as the superconducting film for the fabrication of this structure [69]. The thin Cu layer was deposited on the Pb to protect it from oxidation and to provide a good contact-layer for the wire-bonding to the experimental apparatus. An AFM image of the Pb/Cu 2×2 antidot cluster, is shown in Fig. 17 together with a reference sample (i.e. a Pb/Cu microsquare of 2×2 μm^2 without antidots). The Pb(50 nm)/Cu(50 nm) bilayer behaves as a Type-II superconductor with a $T_{c0} = 6.05\,K$, a coherence length, $\xi(0) \approx 35$ nm and a dirty limit penetration depth, $\lambda(0) \approx 76$ nm. The $T_c(H)$ measurements on the reference sample [68] revealed characteristic features originating from the confinement of the superconducting condensate by the dot geometry (see Section II.C). The additional features observed in the $T_c(H)$ phase boundary of the antidot cluster can therefore be attributed to the presence of the antidots.

The experimental $T_c(H)$ phase boundary is shown in Fig. 18. It was measured by keeping the sample resistance at 10% of its normal state value and varying the magnetic field and temperature [68].

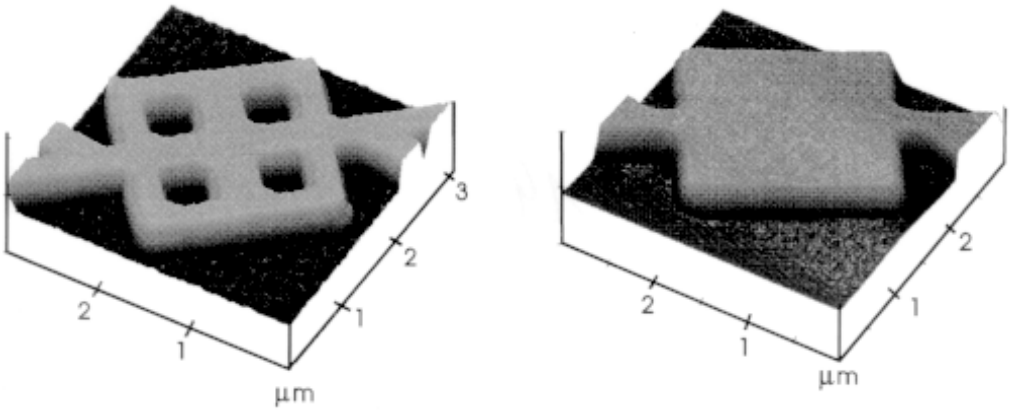

FIGURE 17. AFM image of the Pb/Cu 2×2 antidot cluster (on the left) and of the reference sample (on the right). (adapted from Ref. [68])

Strong oscillations are observed with a periodicity of 2.6 mT and in each of these periods, smaller dips appear at approximately 0.75 mT, 1.3 mT and 1.8 mT. The parabolic background superimposed on $T_c(H)$ can again be described by Eq. (11).

Defining a flux quantum per antidot as $\Phi_0 = h/2e = BS$, where $B = \mu_0 H$ and S is an effective area per antidot cell (S= 0.8 μm^2), the minima observed in the magnetoresistance and the $T_c(H)$ phase boundary at integer multiples of 2.6 mT can be correlated with a magnetic flux quantum per antidot cell, $\Phi = n\Phi_0$. The ones observed at 0.75 mT, 1.3 mT and 1.8 mT correspond to the values Φ/Φ_0=0.3, 0.5 and 0.7.

The solutions obtained from the London model define a phase boundary which is periodic in Φ with a periodicity of Φ_0. Within each parabola $\Delta T_c = \gamma(\Phi/\Phi_0)^2$, where the coefficient γ characterizes the effective flux penetration through the unit cell. The γ-value is determined by the combination of λ and the effective size of the current loops. In Fig. 19, the first period of this phase boundary, $\Delta T_c(\Phi) = T_{c0} - T_c(\Phi)$ versus Φ/Φ_0, is shown. There are six parabolic solutions given by a different set of flux quantum numbers $\{n_i\}$, each one defining a specific vortex configuration. In Fig. 19a, this is indicated by the numbers shown inside the schematic drawings of the antidot cluster. Note that some vortex configurations are degenerate.

From all these possible solutions, for each particular value of Φ/Φ_0, only the branch with a minimum value of $\Delta T_c(\Phi)$ is stable (indicated with a solid line in Fig. 19a). For the phase boundary, calculated within the 1D model of 4 equivalent and properly attached squares, no fitting parameters were used since the variation of $T_c(\Phi)$ was calculated from the known values for ξ and the size. One period of the phase boundary of the antidot cluster is composed of five branches and in each branch a different stable vortex

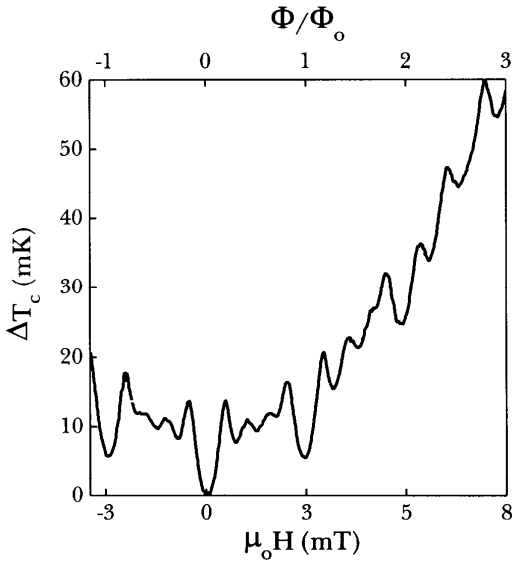

FIGURE 18. Experimental phase boundary, $\Delta T_c(H)$ for the Pb/Cu 2×2 antidot cluster. (adapted from Ref. [68])

configuration is permitted. For the middle branch ($0.37< \Phi/\Phi_0 <0.63$), the stable configuration is the *diagonal* vortex configuration (antidots with equal n_i at the diagonals) instead of the *parallel* state (dashed line in Fig. 19a).

The net supercurrent density distribution circulating in the antidot cluster for different values of Φ/Φ_0 has been determined using the same approach. Circular currents flow around each antidot. For the states n_i=0 and n_i=1 currents flow in the opposite direction, since currents corresponding to n_i=0 must screen the flux to fulfill the fluxoid quantization condition (Eq. (14)), whereas for n_i=1 they have to generate flux. At low values of Φ/Φ_0, currents are canceled in the internal strips and screening currents only flow around the cluster. When the field range corresponding to the second branch of the phase boundary is entered, a vortex (n_i=1) is pinned around one antidot of the cluster (see Fig. 19a). At the third branch, the second vortex enters the structure and is localized in the diagonal. In the fourth branch of the phase boundary the third vortex is pinned in the antidot cluster. And finally, the current distribution for the fifth branch is similar to that of the first branch although currents flow in opposite direction [69].

Figure 19c shows the first period of the measured phase boundary $T_c(\Phi)$ after subtraction of the parabolic background. The first period of the experimental phase boundary is composed of five parabolic branches with minima at Φ/Φ_0 = 0, 0.3, 0.5, 0.7, 1. If we compare it with the theoretical prediction given in Figure 19a, the overall shape can be reproduced although the experimental plot has two major peaks at Φ/Φ_0 = 0.2 and 0.8 whereas the

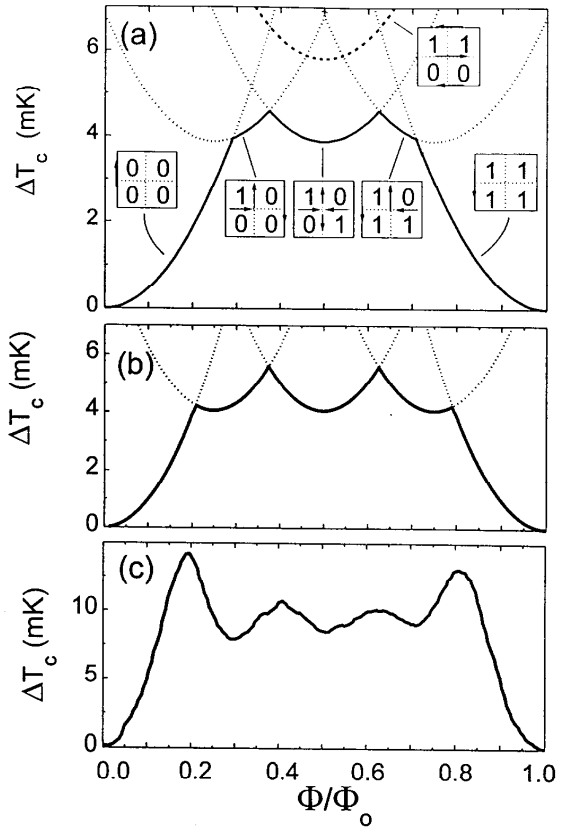

FIGURE 19. (a) Theoretical phase boundary, $T_c(\Phi/\Phi_0)$, calculated in the London limit of the Ginzburg-Landau theory without any fitting parameter (solid line). All possible parabolic solutions are represented by dotted lines. The dashed line indicates the non-stable *parallel* configuration. The schematic representation of the $\{n_i\}$ quantum numbers at the antidots and characteristic current flow patterns for each parabolic branch are also sketched. (b) The $T_c(\Phi/\Phi_0)$ phase boundary, calculated as in Fig. 19a , but with the curvature "γ" of the parabolae taken as a free parameter. The γ-value was increased by a factor of two with respect to its calculated value used in Fig. 19a. (c) First period of the measured phase boundary shown in Fig. 18 after subtraction of the parabolic background. (adapted from Ref. [68])

theoretical curve only predicts cusps around these positions.

The agreement between the measured and the calculated $T_c(\Phi)$ is improved if we assume that the coefficient γ can be considered as a fitting parameter. This seems to be feasible if we take into account the simplicity and limitation of the used 1D model. Due to the relatively large width of the strips forming the 2×2 cluster, the sizes of the current loops can change since they are "soft" in this case and not defined very precisely.

As a result, the coefficient γ can not be treated as a known constant. If we use it as a free parameter (Fig. 19b) then the curvature of all parabolae forming $T_c(H)$ can be changed and the calculated $T_c(H)$ curve becomes closer to the experimental one though the amplitude of the maxima at $\Phi/\Phi_0 = 0.2$ and 0.8 is still lower than in the experiment (Fig. 19c). The discrepancy in the amplitude of the maxima at $\Phi/\Phi_0 = 0.2$ and 0.8 could also be related to the pinning of vortices by the antidot cluster when potential barriers between different vortex configurations may appear. At the same time, the achieved agreement between the positions of the measured and calculated minima of the $T_c(H)$ curves confirms that the observed effects are due to fluxoid quantization and formation of certain stable vortex configurations at the antidots [68,69].

An extrapolation of the results obtained from small to larger 2D antidot clusters (3×3, 4×4, etc.) gives an idea about possible vortex configurations, which can be expected in superconductors with huge regular arrays of antidots (antidot lattices).

IV HUGE ARRAYS OF NANOSCOPIC PLAQUETTES IN LATERALLY NANOSTRUCTURED SUPERCONDUCTORS

The periodic repetition of a certain nanoscopic plaquette A over a macroscopic area makes it possible to implement the idea of an artificial lateral modulation in nanostructured superconductors. Several different types of elementary cells A have been used for that: antidots [70–72,41,73–76] (complete microholes in a film), blind holes [77,78] (no perforation but a thickness modulation at the sites of the blind holes), magnetic [79–82], normal metallic [79], or insulating dots [79] covered by (or grown on top of) a superconducting film. These huge regular arrays of nanoscopic plaquettes can be used for systematic studies of the confinement and quantization phenomena in the presence of a 2D artificial periodic pinning potential. We begin in this section from the effect of lateral nanostructuring on the $T_c(H)$ phase boundary and then briefly discuss pinning phenomena in superconductors with an antidot lattice.

A The $T_c(H)$ phase boundary of superconducting films with an antidot lattice

Superconducting films with a regular array of antidots are convenient model objects to study the effects of the confinement topology on the $T_c(H)$ phase boundary in two different regimes [78]:

(i) The first or "*collective*" regime corresponds to the situation where all elements A, forming an array, are coupled. From the experimental $T_c(H)$ data on antidot clusters we expect for films with an antidot lattice higher critical fields at $\Phi = n\Phi_0$, which is in agreement with the appearance of the $T_c(H)$ cusps at $\Phi = n\Phi_0$ in superconducting networks [83]. Here, the flux Φ is calculated per unit cell of the antidot lattice.

(ii) On the other hand, by applying sufficiently high magnetic fields, the individual circular currents flowing around antidots, can be decoupled and the crossover to a "*single object*" behavior could be observed. In this case the relevant area for the flux is the area of the antidot itself and we deal with surface superconductivity around an antidot.

Figure 20 shows the critical field for a Pb(50 nm) sample with a square antidot lattice (period $d = 1\,\mu$m and the antidot radius $r_a = 0.24\,\mu$m). The $T_c(H)$ boundary is determined at 10% of the normal state resistance, R_n. In this graph two distinct periodicities are present:

(i) Below ~ 8 mT cusps are found with a period of 2.07 mT, corresponding to one flux-quantum per lattice cell. These cusps or "*collective*" oscillations [78] are reminiscent of superconducting wire networks [83] and arize from the phase correlations between the different loops which constitute the network. These cusps are obtained by narrowing the minima at $n\Phi_0$ with increasing size N of the $N \times N$ antidot cluster (see the sharpening of the minima at $\Phi = 0$, Φ_0 in Fig. 21; note that the phase boundary in the $N \to \infty$ case has a similar shape as the lowest energy level of the Hofstadter butterfly [15,84]). An important observation is that the amplitude of these "collective" oscillations depends upon the choice of the resistive criterion. This is similar to the case of Josephson junction arrays and weakly coupled wire networks [86] where phase fluctuations dominate the resistive behavior. The inset of Fig. 20 shows the first collective period, measured using three different criteria. As the criterion is lowered the cusps become sharper and the amplitude increases well above the prediction based on the mean field theory for strongly coupled wire networks [83]. At the same time, cusps appear at rational fields Φ/Φ_0=1/4, 1/3, 1/2, 2/3 and 3/4 arizing from the commensurability of the vortex structure with the underlying lattice.

(ii) Above ~ 8 mT, the collective oscillations die out and "*single object*" cusps appear, having a periodicity which roughly corresponds to one flux quantum Φ_0 per antidot area, r_a^2. These cusps are due to the transition between localized superconducting edge states [78] having a different angular

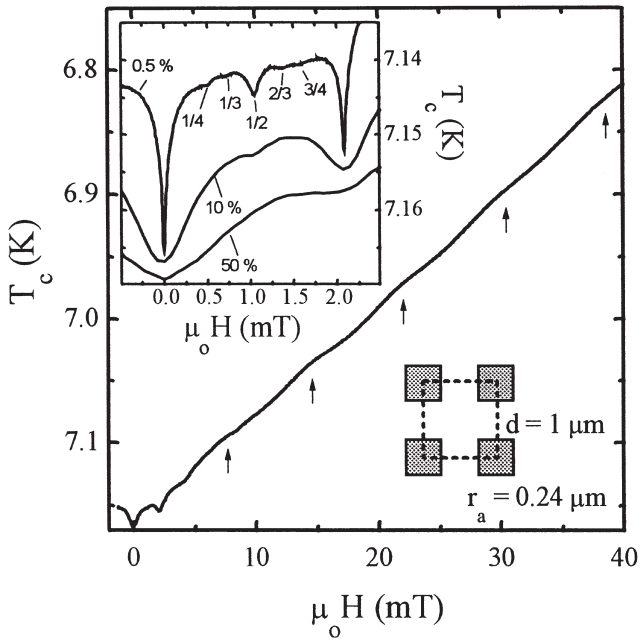

FIGURE 20. Critical field of a superconducting Pb(50 nm) film measured at 10% R_n (R_n is the normal state resistance just above T_c), with $d = 1\ \mu$m, $r_a = 0.24\ \mu$m. The inset shows a zoom of the $T_c(H)$ data determined using different criteria 50% R_n, 10% R_n and 0.5% R_n. (adapted from Ref. [73])

momentum L. These states are formed around the antidots and are, just as the dot in Section II.C, described by an orbital momentum quantum number L.

Figure 22 shows the same critical field as presented in Fig. 20, but normalized by the upper critical field H_{c2} of a plain film without antidots, $\mu_0 H_{c2} = \Phi_0/2\pi\xi^2(T)$ ($\xi(0)$=36 nm). The dashed line is the calculation of the reduced critical field for a plain film with a single circular antidot with radius $r_a = 0.24\ \mu$m. The positions of the cusps correspond reasonably well to the experimental ones, taking into account that the model only considers a single hole. From this comparison, an effective area $\pi r_a^2 = 0.187\ \mu m^2$ is determined which is close to the experimental value $0.16\ \mu m^2$.

From Figures 20 and 22 it is possible to show that the transition from the network regime to the "single object" regime takes place at a temperature T^* approximately given by the relation $w \approx 1.6\,\xi(T^*)$, (where w is the width of the superconducting region between two adjacent antidots) [85].

Experiments on systems with other antidot sizes demonstrate that the r_a/d ratio determines the relative importance of the "collective regime" and changes the cross-over temperature T^*. The relation $w \approx 1.6\,\xi(T^*)$, seems nevertheless

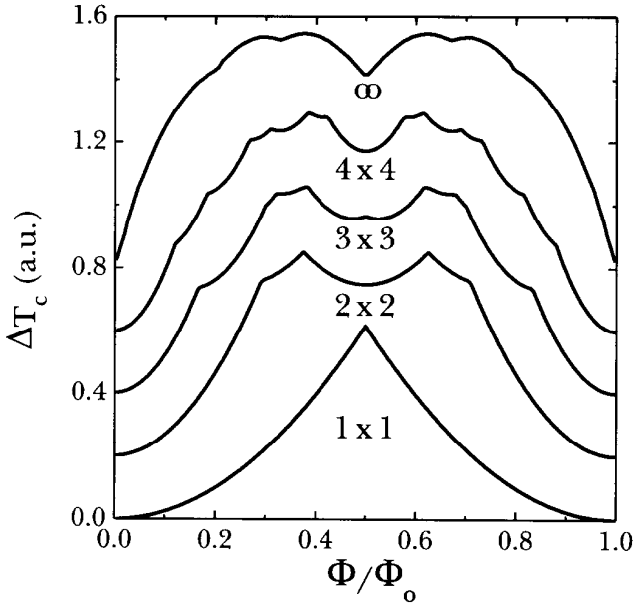

FIGURE 21. Calculations of the first $T_c(H)$ period for an $N \times N$ antidot system ($N = 1, 2, 3, 4, \infty$) in the London limit. The minima at integer Φ/Φ_0 for a single loop ($N = 1$) are transformed to sharp cusps as $N \to \infty$. (adapted from Ref. [85])

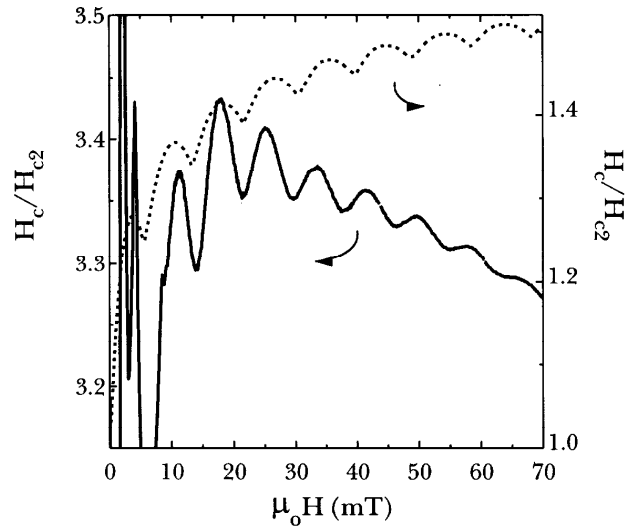

FIGURE 22. The critical field of Fig. 20 normalized by $\Phi_0/2\pi\xi^2(T)$ versus the applied field. The dashed line (right axis) shows the theoretical result [78] for a single circular hole with a radius $r_a = 0.24\,\mu$m.

to hold reasonably well and is similar to the transition from bulk nucleation of superconductivity to surface nucleation in a thin superconducting slab parallel to the magnetic field [40], which happens at a temperature T_{cr} satisfying $w = 1.8\,\xi(T_{cr})$.

Comparing the bulk $H_{c2}(T)$ curve with the $T_c(H)$ boundary for films with an antidot lattice, we clearly see a qualitative difference between the two, caused by the lateral nanostructuring. For a superconducting network, $T_c(H)$ can be related to the lowest E_{LLL} level in the Hofstadter butterfly [15,84] with pronounced cusps at $n\Phi_0$ and a substructure within each period. In the case of an antidot lattice, the size of the antidots is substantially smaller in compared to a network. Here as well, $T_c(H)$ is substantially modified, but the cusps at $n\Phi_0$ are still clearly seen [73].

Besides a substantial increase in $T_c(H)$, lateral nanostructuring can also be used to optimize flux pinning in order to enhance j_c up to its theoretical limit - the depairing current. We would like to emphasize the unique possibilities to stabilize novel flux phases in superconducting films by making regular arrays of pinning centers (antidots or magnetic dots). These phases are (for further details we refer to Ref. [87]) :

(i) *Multiquanta vortex lattices.* They can be realized if the antidots are sufficiently large and field does not exceed the value H_{n_s} defined by the saturation number $n_s \approx r_a/2\xi(T)$ [88]. This saturation number defines the maximum number of vortices which can be trapped by an antidot with radius r_a.

(ii) *Composite flux lattices.* These flux lattices are observed when the normalized radii of the antidots $r_a/2\xi(T)$ are sufficiently small and H exceeds the limiting field H_{n_s}. Also the pinning potential at interstices should not be very shallow to provide a weaker, but still sufficient pinning to form a softer interstitial flux solid. The composite flux lattices are characterized by the coexistence of the two-weakly and strongly pinned-interpenetrating flux lattices at interstices (Φ_0 vortices) and antidots ($n\Phi_0$ vortices), respectively. [70,89]

(iii) *Multiquanta vortex lattice coexisting with the interstitial fluid of* Φ_0 *vortices.* This flux phase is formed when $T \to T_c$ and the interstitial pinning potential becomes very shallow and thus cannot prevent the melting of the caged interstitial pinning Φ_0 vortices.

The flux phases listed above can exist at temperatures not too far from T_c, when a "single terrace" critical state is established [76]. At lower temperatures the tendency to form a conventional Bean profile starts to dominate and matching anomalies are suppressed, for example for Pb/Ge, any $M(H)$ matching anomalies below 5 K can barely be seen.

Since in superconductors with antidot lattices the vortex confinement is well-controlled, it is interesting to use them as a model system to study the problem of the "optimum pinning". The systematic measurements of the efficiency of antidots, as artificial pinning centers, as a function of their radius r_a (Fig. 23) have revealed [76] that for core pinning combined with the electromagnetic pinning the optimum size of the antidots is not $\xi(T)$ at all, but

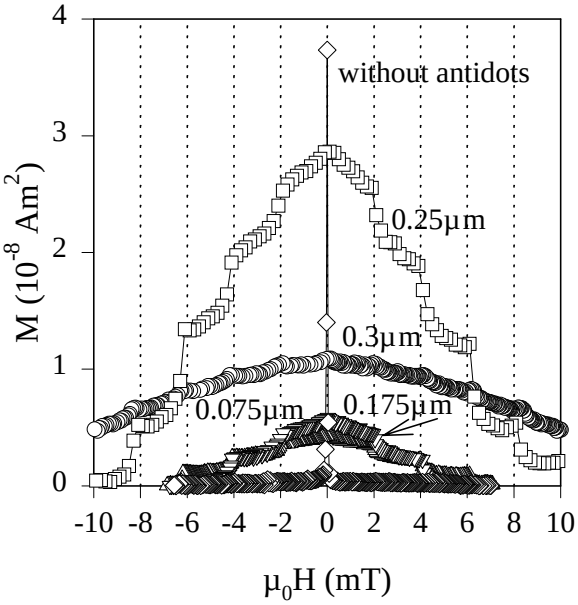

FIGURE 23. Magnetization curves ($T = 0.98\ T_c$) of a single WGe(60 nm) film with a square lattice of antidots with radius $r_a = 0.075 - 0.3\ \mu$m. For comparison, the data for the reference multilayers without antidots are also shown. The matching fields $\mu_0 H_n \approx n \times 2.07$ mT (where n is an integer) are indicated by dashed lines. (adapted from Ref. [76])

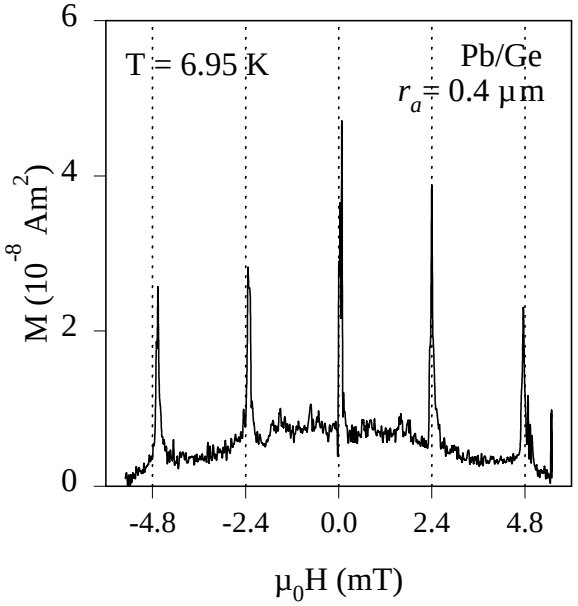

FIGURE 24. Upper magnetization curve at $T = 6.95$ K of the [Pb(15 nm)/Ge(14 nm)]$_3$] multilayer with a triangular antidot lattice ($r_a = 0.4\,\mu$m). (adapted from Ref. [76])

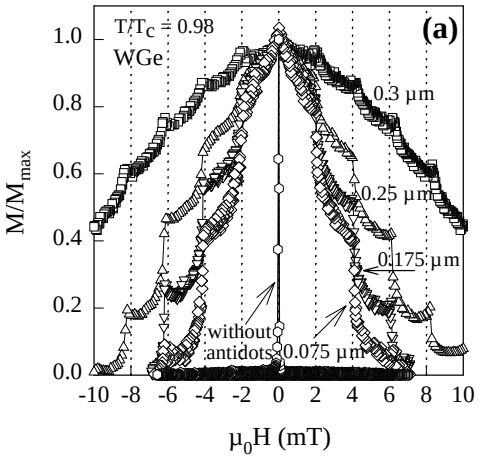

FIGURE 25. (a) Normalized magnetization curves ($T = 0.98\,T_c$) of a single WGe(60 nm) film with a square lattice of antidots with radius $r_a = 0.075 - 0.3\,\mu$m. For comparison, the data for the reference multilayers without antidots are also shown. The matching fields $\mu_0 H_n \approx n \times 2.07$ mT (where n is an integer) are indicated by dashed lines.

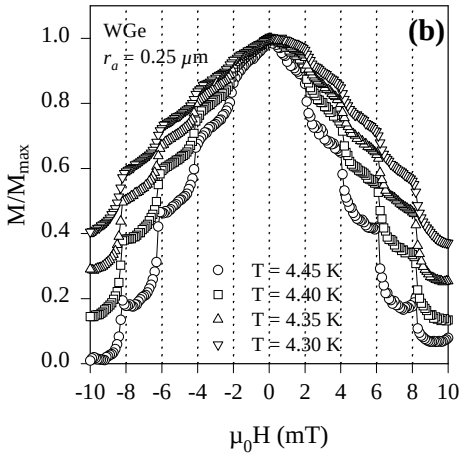

FIGURE 25. (b) Magnetization curves at different temperatures of a single WGe(60 nm) film with a square lattice of antidots with radius $r_a = 0.25\,\mu$m. The matching fields $\mu_0 H_n \approx n \times 2.07$ mT (where n is an integer) are indicated by dashed lines. (adapted from Ref. [76])

rather $2r_a \gg \xi(T)$ [76,90]. As a result, the highest critical currents have been obtained for the multiquanta vortex lattices that can be stabilized by these sufficiently large antidots, since their saturation number is $n_s \approx r_a/2\xi(T) \gg 1$. At the same time it is quite evident that by increasing the antidot diameter we are inducing a crossover to another regime (Fig. 24) when eventually $2r_a$ becomes nearly the same as the antidot lattice period d. In this case the width of the superconducting strips w between the antidots is so small that at temperatures not too far below T_c the superconducting network regime $w \leq \xi(T)$ can be realized.

For this regime the M vs. H curves are characterized by the presence of sharp peaklike anomalies at integer matching fields H_n (Fig. 24) and a reproducible structure between H_n, which may correspond to rational matching peaks. Both integer and rational matching peaks have been observed before in various superconducting networks [15] and Josephson networks [91]. Visually the $M(H)$ curves in the *network regime* are quite different from those in the *multiquanta vortex regime*: the former demonstrate the $M(H)$ peaks at $H = H_n$ (Fig. 24), while the latter show pronounced cusps at integer matching fields (Fig. 25b).

In the regime of a superconducting network, critical currents in moderate fields are already substantially smaller than for the regime of the multiquanta vortex lattices (see Fig. 23). At higher fields, however, at least for the radius $r_a = 0.3$ μm, critical currents are higher for the largest studied antidot diameter, i.e., *the optimum antidot size for pinning is field-dependent.* The reduction of the width of the superconducting "stripes" between the antidots, needed to obtain high j_c in high fields, reflects actually a well-known designer rule for making superconducting cables, which usually consist of a bunch of very fine superconducting filaments embedded into a normal metallic matrix. Therefore, *the optimum size* of the pinning centers turns out to be *field dependent*: smaller antidots are more efficient in low fields, while in higher fields larger antidots are needed to optimize j_c.

Summarizing briefly the analysis of the multiquanta vortices, it is worth noting that the superconducting film with a lattice of relatively large antidots seems to demonstrate the single-terrace critical state which appears due to the multiple connectivity of the film and the stabilization of the $n\Phi_0$-flux lattices. *The separation of the areas where flux penetrates from those where the superconducting order parameter nucleates provides a kind of a "peaceful coexistence" of FL's pinned by antidots with the superconducting condensate in the space between them. Fabricating an antidot lattice to let flux go through, we are thus helping the order parameter between the antidots to sustain much higher currents and magnetic fields.*

V CONCLUSIONS

We have carried out a systematic analysis of quantization and confinement phenomena in nanostructured superconductors. The main idea of this study was to vary the boundary conditions for confining the superconducting condensate by taking samples of different topology and, through that, to modify the lowest Landau level $E_{LLL}(H)$ and therefore the critical temperature $T_c(H)$. Three different types of samples were used: (i) individual nanostructures (lines, loops, dots), (ii) clusters of nanoscopic elements - 1D clusters of loops and 2D clusters of antidots, and (iii) films with huge regular arrays of antidots (antidot lattices). We have shown that in all these structures, the phase boundary $T_c(H)$ changes dramatically when the confinement topology for the superconducting condensate is varied. The induced $T_c(H)$ variation is very well described by the calculations of $E_{LLL}(H)$ taking into account the imposed boundary conditions. These results convincingly demonstrate that the phase boundary in $T_c(H)$ of nanostructured superconductors differs drastically from that of corresponding bulk materials. Moreover, since, for a known geometry, $E_{LLL}(H)$ can be calculated a priori, the superconducting critical parameter, i.e. $T_c(H)$, can be controlled by designing a proper confinement geometry. While before, the optimization of the superconducting critical parameters has been done mostly by looking for different materials, we now have a unique alternative - to improve the superconducting critical parameters of *the same material* through the optimization of *the confinement topology* for the superconducting condensate and for the penetrating magnetic flux.

The critical current enhancement due to the presence of the antidots, used as artificial pinning arrays, has been analyzed. Different pinning regimes can be distinguished in dependence upon the antidot diameter. Controlling the periodic pinning potential through lateral nanostructuring, the critical current density $j_c(H)$ can be eventually enhanced up to the theoretical limit - the depairing current. Therefore, the two important superconducting critical parameters, $T_c(H)$ and $j_c(H)$, can be drastically improved by using the concept of "quantum design" : creating the proper confinement topology for the superconducting condensate and the penetrating flux lines to optimize $T_c(H)$ and $j_c(H)$.

ACKNOWLEDGMENTS

The authors would like to thank E. Rosseel, M. Baert, K. Temst, T. Puig, V. Metlushko, C. Strunk, J.G. Rodrigo, X. Qiu, A. Tonomura, C. Van Haesendonck, A. López, H. Fink, S. Haley, A. Buzdin, J. Devreese, V. Fomin, and F. Peeters for fruitful discussions. We are grateful to the Flemish Fund for Scientific Research (FWO), the Flemish Concerted Action (GOA), the Belgian Inter-University Attraction Poles (IUAP), the bilateral TOURNESOL

1998 programme and the ESF "VORTEX" Program for the financial support. M. J. Van Bael is a Post-Doctoral Research Fellow of the FWO.

REFERENCES

1. V. V. Moshchalkov, V. Bruyndoncx, E. Rosseel, L. Van Look, M. Baert, M. J. Van Bael, T. Puig, C. Strunk, and Y. Bruynseraede, in *Lectures on Superconductivity in Networks and Mesoscopic systems*, edited by C. Giovannella and C. J. Lambert, (AIP Conference Proceedings 427, New York, 1998).
2. C. S. L. Chun, G.-G. Zheng, J. L. Vicent, and I. K. Schuller, Phys. Rev. B **29**, 4915 (1984).
3. K. Kanoda, H. Mazaki, N. Hosoito, and T. Shinjo, Phys. Rev. B **35**, 6736 (1987).
4. V. I. Dediu, V. V. Kabanov, and A. S. Sidorenko, Phys. Rev. B **49**, 4027 (1994).
5. H. K. Wong, B. Y. Jin, H. Q. Yang, J. B. Ketterson, and J. E. Hilliard, J. Low Temp. Phys. **63**, 307 (1986).
6. P. Koorevaar, Y. Suzuki, R. Coehoorn, and J. Aarts, Phys. Rev. B **49**, 441 (1994).
7. C. Strunk, C. Sürgers, U. Paschen, and H. von Löhneysen, Phys. Rev. B **49**, 4053 (1994).
8. J. S. Jiang, D. Davidovic, D. H. Reich, and C. L. Chien, Phys. Rev. Lett. **74**, 314 (1995).
9. Th. Mühge, N. N. Garif′yanov, Yu. V. Goryunov, G. G. Khaliullin, L. R. Tagirov, K. Westerholt, I. A. Garifullin, and H. Zabel, Phys. Rev. Lett. **77**, 1857 (1996).
10. J. Aarts, J. M. E. Geers, E. Brück, A. A. Golubov, and R. Coehoorn, Phys. Rev. B **56**, 2779 (1997).
11. J. E. Mattson, C. H. Sowers, A. Berger, and S. D. Bader, Phys. Rev. Lett. **68**, 3252 (1992).
12. G. Verbanck, C. D. Potter, V. Metlushko, R. Schad, V. V. Moshchalkov, and Y. Bruynseraede, Phys. Rev. B **57**, 6029 (1998).
13. Z. Radovic, L. Dobrosavljevic-Grujic, A. I. Buzdin, and J. R. Clem, Phys. Rev. B **44**, 759 (1991).
14. K. Ensslin, and P. M. Petroff, Phys. Rev. B **41**, 12307 (1990); H. Fang, R. Zeller, and P. J. Stiles, Appl. Phys. Lett. **55**, 1433 (1989); R. Schuster, K. Ensslin, D. Wharam, S. Kühn, J. P. Kotthaus, G. Böhm, W. Klein, G. Tränkle, and G. Weimann, Phys. Rev. B **49**, 8510 (1994).
15. B. Pannetier, J. Chaussy, R. Rammal, and J. C. Villegier, Phys. Rev. Lett. **53**, 1845 (1984).
16. V. V. Moshchalkov, L. Gielen, C. Strunk, R. Jonckheere, X. Qiu, C. Van Haesendonck, and Y. Bruynseraede, Nature **373**, 319 (1995).
17. M. Tinkham, Phys. Rev. **129**, 2413 (1963).
18. P. G. de Gennes, *Superconductivity of Metals and Alloys*, Benjamin, New York (1966).

19. J. Romijn, T. M. Klapwijk, M. J. Renne, and J. E. Mooij, Phys. Rev. B **26**, 3648 (1982).
20. H. Welker, and S. B. Bayer, Akad. Wiss. **14**, 115 (1938).
21. M. Tinkham, *Introduction to Superconductivity*, McGraw Hill, New York (1975).
22. W. A. Little, and R. D. Parks, Phys. Rev. Lett. **9**, 9 (1962); R. D. Parks, and W. A. Little, Phys. Rev. **133**, A97 (1964).
23. R. P. Groff, and R. D. Parks, Phys. Rev. **176**, 567 (1968).
24. X. Zhang and J. C. Price, Phys. Rev. B **55**, 3128 (1997).
25. R. Benoist and W. Zwerger, Z. Phys. B **103**, 377 (1997).
26. C. Strunk, V. Bruyndoncx, V. V. Moshchalkov, C. Van Haesendonck, Y. Bruynseraede, and R. Jonckheere, Phys. Rev. B **54**, R12701 (1996).
27. P.-G. de Gennes, C. R. Acad. Sci. Ser. II **292**, 279 (1981).
28. V. M. Fomin, V. R. Misko, J. T. Devreese, and V. V. Moshchalkov, Solid State Commun. **101**, 303 (1997).
29. V. M. Fomin, J. T. Devreese, and V. V. Moshchalkov, Europhys. Lett. **42**, 553 (1998).
30. E. M. Horane, J. I. Castro, G. C. Buscaglia, and A. López, Phys. Rev. B **53**, 9296 (1996).
31. J. Berger and J. Rubinstein, Phys. Rev. Lett. **75**, 320 (1995).
32. J. Berger and J. Rubinstein, Phil. Trans. R. Soc. Lond. A **355**, 1969 (1997).
33. J. Berger and J. Rubinstein, Physica C **288**, 105 (1997).
34. J. Berger and J. Rubinstein, Phys. Rev. B **56**, 5124 (1997).
35. R. B. Dingle, Proc. R. Soc. London, Ser. A **211**, 500 (1952).
36. V. V. Moshchalkov, M. Dhallé, and Y. Bruynseraede, Physica C **207**, 307 (1993).
37. D. Saint-James, Phys. Lett. **15**, 13 (1965); O. Buisson, P. Gandit, R. Rammal, Y. Y. Wang, and B. Pannetier, Phys. Lett. A **150**, 36 (1990).
38. V. V. Moshchalkov, X. G. Qiu, and V. Bruyndoncx, Phys. Rev. B **55**, 11793 (1996).
39. K. Nakamura and H. Thomas, Phys. Rev. Lett. **61**, 247 (1988).
40. D. Saint-James, Phys. Lett. **16**, 218 (1965).
41. V. V. Moshchalkov, L. Gielen, M. Baert, V. Metlushko, G. Neuttiens, C. Strunk, V. Bruyndoncx, X. Qiu, M. Dhallé, K. Temst, C. Potter, R. Jonckheere, L. Stockman, M. Van Bael, C. Van Haesendonck, and Y. Bruynseraede, Physica Scripta **T55**, 168 (1994).
42. P. S. Deo, V. A. Schweigert, F. M. Peeters, and A. K. Geim, Phys. Rev. Lett. **79**, 4653 (1997).
43. V. A. Schweigert and F. M. Peeters, Phys. Rev. B **57**, 13817 (1998).
44. J. J. Palacios, Phys. Rev. B. **58**, R5948 (1998).
45. A. K. Geim, I. V. Grigorieva, S. V. Dubonos, J. G. S. Lok, J. C. Maan, A. E. Filippov, and F. M. Peeters, Nature **390**, 259 (1997).
46. A. K. Geim, S. V. Dubonos, J. G. S. Lok, I. V. Grigorieva, J. C. Maan, L. Theil Hansen, and P. E. Lindelof, Appl. Phys. Lett. **71**, 2379 (1997).
47. A. K. Geim, S. V. Dubonos, I. V. Grigorieva, J. G. S. Lok, J. C. Maan, X. Q. Li,

and F. M. Peeters, Superlatt. Microstruct. **23**, 151 (1998).
48. A. I. Buzdin and J. P. Brison, Phys. Lett. A **196**, 267 (1994).
49. V. Bruyndoncx, C. Strunk, V. V. Moshchalkov, C. Van Haesendonck, and Y. Bruynseraede, Europhys. Lett. **36**, 449 (1996).
50. S. Alexander, and E. Halevi, J. Phys. (Paris) **44**, 805 (1983).
51. C. C. Chi, P. Santhanam, and P. E. Blöchl, J. Low Temp. Phys. **88**, 163 (1992).
52. S. Alexander, Phys. Rev. B **27**, 1541 (1983).
53. C. Ammann, P. Erdös, and S. B. Haley, Phys. Rev. B **51**, 11739 (1995).
54. J. I. Castro, and A. López, Phys. Rev. B **52**, 7495 (1995).
55. R. D. Parks, Science **146**, 1429 (1964).
56. J. Simonin, D. Rodrigues, and A. López, Phys. Rev. Lett. **49**, 944 (1982).
57. H. J. Fink and S. B. Haley, Phys. Rev. B **43**, 10151 (1991).
58. H. J. Fink and V. Grünfeld, Phys. Rev. B **31**, 600 (1985).
59. H. J. Fink, O. Buisson, and B. Pannetier, Phys. Rev. B **43**, 10144 (1991).
60. H. J. Fink, Phys. Rev. B **45**, 4799 (1992); erratum in Phys. Rev. B **48**, 3579 (1993).
61. S. B. Haley and H. J. Fink, Phys. Lett. A **102**, 431 (1984).
62. H. J. Fink and S. B. Haley, Phys. Rev. Lett. **66**, 216 (1991).
63. J. M. Simonin, C. Wiecko, and A. López, Phys. Rev. B **28**, 2497 (1983).
64. T. M. Larson and S. B. Haley, Phyica B **194-196**, 1425 (1994).
65. T. M. Larson and S. B. Haley, Appl. Supercond. **3**, 573 (1995).
66. T. M. Larson and S. B. Haley, J. Low Temp. Phys. **107**, 3 (1997).
67. H. J. Fink, A. López, and R. Maynard, Phys. Rev. B **26**, 5237 (1982).
68. T. Puig, E. Rosseel, M. Baert, M. J. Van Bael, V. V. Moshchalkov, and Y. Bruynseraede, Appl. Phys. Lett. **70**, 3155 (1997).
69. T. Puig, E. Rosseel, L. Van Look, M. J. Van Bael, V. V Moshchalkov, Y. Bruynseraede, and R. Jonckheere, Phys. Rev. B **58**, 5744 (1998).
70. M. Baert, V. V. Metlushko, R. Jonckheere, V. V. Moshchalkov, and Y. Bruynseraede, Phys. Rev. Lett. **74**, 3269 (1995).
71. M. Baert, V. V. Metlushko, R. Jonckheere, V. V. Moshchalkov, and Y. Bruynseraede, Europhys. Lett. **29**, 157 (1995).
72. V. V. Moshchalkov, M. Baert, V. V. Metlushko, E. Rosseel, M. J. Van Bael, K. Temst, R. Jonckheere, and Y. Bruynseraede, Phys. Rev. B **54**, 7385 (1996).
73. E. Rosseel, T. Puig, M. Baert, M. J. Van Bael, V. V. Moshchalkov, and Y. Bruynseraede, Physica C **282-287**, 1567-1568 (1997).
74. A. F. Hebard, A. T. Fiory, and S. Somekh, IEEE Trans. Magn. **1**, 589 (1977).
75. V. Metlushko, L. E. DeLong, M. Baert, E. Rosseel, M. J. Van Bael, K. Temst, V. V. Moshchalkov, and Y. Bruynseraede, Europhys. Lett. **41**, 333 (1998).
76. V. V. Moshchalkov, M. Baert, V. V. Metlushko, M. J. Van Bael, K. Temst, R. Jonckheere, and Y. Bruynseraede, Phys. Rev. B **57**, 3615 (1998).
77. A. Bezryadin and B. Pannetier, J. Low Temp. Phys. **102**, 73 (1996).
78. A. Bezryadin, and B. Pannetier, J. Low Temp. Phys. **98**, 251 (1996);
A. Bezryadin, A. Buzdin, and B. Pannetier, Phys. Rev. B **51**, 3718 (1995).
79. M. J. Van Bael, *Regular arrays of magnetic dots and their flux pinning properties*, Ph. D. thesis, K.U.Leuven (1998).

80. J. I. Martín, M. Vélez, J. Nogués, and I. K. Schuller, Phys. Rev. Lett. **79**, 1929 (1997).
81. M. J. Van Bael, K. Temst, V. V. Moshchalkov, Y. Bruyseraede, Phys. Rev. B **59**, 14 674 (1998).
82. M. J. Van Bael, L. Van Look, K. Temst, M. Lange, J. Bekaert, U. May, G. Güntherodt, V. V. Moshchalkov, Y. Bruynseraede, Physica C (2000) *in press.*
83. B. Pannetier, in *Quantum coherence in mesoscopic systems*, edited by B. Kramer, Plenum Press, New York (1991).
84. D. R. Hofstadter, Phys. Rev. B **14**, 2239 (1976).
85. E. Rosseel, *Critical parameters of superconductors with an antidot lattice*, Ph. D. thesis, K.U.Leuven (1998).
86. M. Giroud, O. Buisson, Y. Y. Wang, B. Pannetier, and D. Mailly, J. Low Temp. Phys. **87**, 683 (1992); H. S. J. van der Zant, M. N. Webster, J. Romijn, and J. E. Mooij, Phys. Rev. B **50**, 340 (1994).
87. V. V. Moshchalkov, V. Bruyndoncx, L. Van Look, M. J. Van Bael, Y. Bruynseraede, A. Tonomura in *Handbook of Nanostuctured materials and Nanotechnology*, edited by H. S. Nalwa, Academic Press (2000), Vol. 3, Chapter 9, p. 451-525.
88. G. S. Mkrtchyan and V. V. Schmidt, Sov. Phys. JETP **34**, 195 (1972).
89. E. Rosseel, M. Van Bael, M. Baert, R. Jonckheere, V. V. Moshchalkov, and Y. Bruynseraede, Phys. Rev. B **53**, R2983 (1996).
90. V. V. Moshchalkov, M. Baert, V. V. Metlushko, E. Rosseel, M. Van Bael, K. Temst, X. Qiu, R. Jonckheere, and Y. Bruynseraede, Jpn. J. Appl. Phys. **34**, 4459 (1995).
91. W. J. Elion, H. S. J. Van der Zant, and J. E. Mooij, *Macroscopic Quantum Phenomena and Coherence in Superconducting Networks*, World Scientific, Singapore, p. 105 (1995).